J. Fluid Mech. (2010), *vol.* 657, *pp.* 502–538. © Cambridge University Press 2010
doi:10.1017/S0022112010001795

Decay of magnetohydrodynamic turbulence at low magnetic Reynolds number

P. BURATTINI[1]†, O. ZIKANOV[2] AND B. KNAEPEN[1]

[1]Physique Statistique et des Plasmas, Université Libre de Bruxelles, B-1050 Brussels, Belgium

[2]Department of Mechanical Engineering, University of Michigan, Dearborn, MI 48128-1491, USA

(Received 20 October 2009; revised 9 April 2010; accepted 11 April 2010;

We report a detailed numerical investigation of homogeneous decaying turbulence in an electrically conducting fluid in the presence of a uniform constant magnetic field. The asymptotic limit of low magnetic Reynolds number is assumed. Large-eddy simulations with the dynamic Smagorinsky model are performed in a computational box sufficiently large to minimize the effect of periodic boundary conditions. The initial microscale Reynolds number is about 170 and the magnetic interaction parameter N varies between 0 and 50. We find that except for a short period of time when $N = 50$, the flow evolution is strongly influenced by nonlinearity and cannot be adequately described by any of the existing theoretical models. One particularly noteworthy result is the near equipartition between the rates of Joule and viscous dissipations of the kinetic energy observed at all values of N during the late stages of the decay. Further, the velocity components parallel and perpendicular to the magnetic field decay at different rates, whose value depends on the strength of the magnetic field and the stage of the decay. This leads to a complex evolution of the Reynolds stress anisotropy ellipsoid, which goes from being rod-shaped, through spherical to disc-shaped. We also discuss the possibility of the power-law decay, the comparison between computed, experimental and theoretical decay exponents, the anisotropy of small-scale fluctuations, and the evolution of the spectral energy distributions.

Key words: MHD turbulence

1. Introduction

The decay of homogeneous isotropic turbulence (HIT) has been extensively considered in the literature. It has both practical significance – e.g. for the calibration of the k–ϵ model coefficients (George *et al.* 2001) – and fundamental implications for the understanding of turbulence (Pope 2000). In this context, two points are particularly relevant: the establishment of a power-law decay of the turbulent kinetic energy and its decay rate. Although there is a general agreement, which is also supported by self-similarity arguments, that the decay follows a power law, the quantification of the decay exponent has proved elusive. The availability of direct numerical simulations (DNS) at higher resolution has recently renewed the focus on this problem (Ishida, Davidson & Kaneda 2006).

A more general case of homogeneous turbulence is characterized by directional anisotropy. This can in particular be observed in an electrically conductive fluid

---

† Email address for correspondence: paolo.burattini@ulb.ac.be

flowing in the presence of a uniform external magnetic field $\boldsymbol{B}_0$. Practical examples include crystal growth in semiconductors, molten metals in metallurgy and lithium cooling blankets for future fusion reactors. In these and other circumstances, the magnetic field induced by the electric currents in the liquid metal is negligible, in comparison to that imposed externally. The magnetic Reynolds number being small, the quasi-static approximation (Roberts 1967) can be used to simplify the expression of the Lorentz force. According to this approximation, the flow is characterized by two non-dimensional parameters: the hydrodynamic Reynolds number Re and the magnetic interaction parameter N (or alternatively the Hartmann number $Ha = (ReN)^{1/2}$). N represents the ratio of the Lorentz force to inertia. Hereafter, the combination of low magnetic Reynolds number, uniform magnetic field and quasi-static approximation are always assumed, when referring to magnetohydrodynamic (MHD) turbulence of liquid metals.

Our understanding of decaying MHD turbulence remains incomplete. The paucity of detailed data on the decay properties of MHD turbulence is partly due to the anisotropy, which complicates the analytical treatment, and partly due to the complexity of the experiments reproducing such a case. Progress was nonetheless made by Moffatt (1967), who considered the early stages of the decay of the velocity fluctuations after sudden application of a magnetic field of large intensity (i.e. $N \gg 1$). His analysis assumed a linear regime and, therefore, was valid only for a short time after the application of $\boldsymbol{B}_0$, well before nonlinear interactions arise. Moffatt (1967) showed that the magnetic field introduced an imbalance between the different velocity components: the kinetic energy of the velocity parallel to the magnetic field becomes twice that of the velocities in the perpendicular directions. He also showed that the Fourier modes of the fluctuating velocity were more effectively damped along the direction of the magnetic field. The prediction was made that the kinetic energy would decay according to the power law $t^{-1/2}$ for times t much smaller than one eddy turnover time. Due to the linearity hypothesis, however, this temporal limitation precluded any prediction in the so-called initial period of the decay. Here, we follow the classification of stages of freely decaying HIT. It includes the early and late phases, during which the nonlinear term is negligible, and the initial period, during which the nonlinear term is relevant and the energy power spectra are self-similar (Batchelor 1967). Incidentally, the ‘final period’ of decay of MHD turbulence was considered by Lehnert (1955).

Moffatt’s (1967) prediction was tested by Schumann (1976) with DNS. He solved the linearized and fully nonlinear MHD equations of motion over a period of two eddy turnover times for $N = 0$, 1, 5, 50; the spatial resolution was limited to 32^3 Fourier modes. Although the linear approximation was found to be qualitatively valid, it underestimated the effect of $\boldsymbol{B}_0$, even within the first eddy turnover time. As for the dimensionality of the flow, Schumann (1976) concluded that a quasi- but not perfect two-dimensional state could be achieved. This remark was based on the observation that at the end of the simulation, the derivative skewness did not approach zero (as in two-dimensional turbulence).

Kolesnikov & Tsinober (1972) were the first to experimentally investigate the decay of velocity fluctuations in duct flow. The fluid (mercury) was pushed through a grid consisting of parallel bars aligned to the external magnetic field. Measurements of the streamwise velocity component (hence perpendicular to $\boldsymbol{B}_0$) and of the scalar diffusion from a point source were reported. Without magnetic field, the streamwise velocity was rather uniform in the lateral direction, as in classical grid turbulence experiments. The velocity isotropy, which might have been biased by the parallel bars arrangement, was not documented. Kolesnikov & Tsinober (1972) concluded that the magnetic field slowed down the decay rate of the velocity fluctuations and rendered the scalar transport anisotropic. Furthermore, the transport increased in the direction perpendicular to $\boldsymbol{B}_0$.

Alemany *et al.* (1979) carried out an in-depth investigation of MHD grid turbulence. Their case is the experimental analogue of the present simulations and therefore is described in some detail here. The set-up consisted of a biplane grid moving in one direction inside a column of still mercury. Such arrangement is equivalent to that in grid turbulence experiments (e.g. Comte-Bellot & Corrsin 1971), with the difference that in the latter, the grid is stationary and the fluid is moved by a fan. The mercury was immersed in a uniform magnetic field, parallel to the direction of grid motion. Different values of $\boldsymbol{B}_0$ were tested, with N varying from 0.1 to 1.36. The velocity parallel to $\boldsymbol{B}_0$ was measured at several distances x from the grid, ranging from 0 to 19 mesh sizes M. Alemany *et al.* (1979) found that following the application of the magnetic field, the decay exponent m of the power law $u'^2 \sim x^{-m}$ (u' is the velocity fluctuation r.m.s.) increased to 1.7, from $m = 1$ at $\boldsymbol{B}_0 = 0$. Furthermore, m was almost independent of N. Remarkably, the effect of $\boldsymbol{B}_0$ on the decay was opposite to that found by Kolesnikov & Tsinober (1972).

The dimensionality of MHD turbulence was considered by Sommeria & Moreau (1982) (see also Moreau 1990). They tried to reconcile the disagreement between earlier observations in duct flow and grid turbulence of Alemany *et al.* (1979). In the first case, the flow was substantially two-dimensional – the fluctuating velocity component parallel to $\boldsymbol{B}_0$ being much smaller than the other two – while in the second case the fluctuations were rather three-dimensional. The proposed explanation hinged on the effect of the boundary conditions at the electrically insulating walls of the duct. Similar arguments were proposed by Müller & Bühler (2001), who reviewed the available data on grid turbulence in the presence of a magnetic field.

Small-scale properties of homogeneous MHD turbulence were considered by Zikanov & Thess (1998). They reported DNS results for the turbulent flow in a periodic box with large-scale forcing. The main goal was to understand the transformation of statistically steady turbulence under the impact of an imposed magnetic field. The results showed, *inter alia*, an intermittency between two-dimensional and three-dimensional states. A similar configuration of statistically stationary turbulence was used by Vorobev *et al.* (2005), who performed both direct and large-eddy simulations (LES). The focus was on local anisotropy, which was quantified by examining some of the components of the dissipation rate tensor. Albeit the distribution of the Reynolds stress anisotropy invariants was also briefly discussed, the conclusions on that point could not be considered conclusive, since the forcing must have had a significant role in the invariants behaviour.

Knaepen & Moin (2004) performed LES and DNS of decaying homogeneous MHD turbulence and showed that the magnetic field advanced to earlier times the beginning of the decay of the total kinetic energy. This effect is consistent with the nature of the Joule dissipation, which acts immediately at all scales and does not require the development of small-scale structures through the turbulent cascade. They also visualized, for large values of N, the tendency towards two-dimensionality – with the parallel fluctuating component of the velocity tending to zero – and consequent anisotropy of the velocity components. Detailed decay properties (e.g. the power-law exponent) were not reported, as the main objective was to assess LES against DNS. In this respect, the validity of the dynamic Smagorinsky model for simulating temporally decaying MHD turbulence was ascertained. Very recently, Ishida & Kaneda (2007) (see also Burattini *et al.* 2008*b*) investigated the spectral scaling properties of turbulence at small values of N. Assuming that the magnetic field introduced only a small perturbation to the scales within the inertial range, these authors argued that the modified scaling range had a slope of $-7/3$ (instead of Kolmogorov's $-5/3$). This was supported by DNS data at $N = 1$ obtained with large-scale forcing.

A different view of decaying MHD turbulence was taken by Davidson (1995, 1997) (see also Davidson 2001). He analysed a flow in a sphere, assuming that viscous dissipation was negligible compared to Joule dissipation. Under this condition, the component of the global angular momentum of the flow parallel to the magnetic field is conserved, which imposes a lower limit on the total energy of the system. This implies that the flow decays towards a condition of zero Joule dissipation, for which the flow variables are uniform along the magnetic field lines (two-dimensional state). Davidson (1997, 2001) also proposed an analogue of the Kolmogorov decay law for MHD turbulence at low R_m. The theory presupposes that viscous and Joule dissipations are respectively proportional to $u'^3/L_\perp$ and $u'^2(L_\perp/L_\parallel)^2/\tau$. Here, $L_\perp$ and $L_\parallel$ are the relevant length scales across and along the magnetic field, and τ is the magnetic damping time. His analysis suggests that $u'^2L_\parallel L_\perp^4$ is invariant during the decay, similarly to the so-called Loitsyansky's invariant in homogeneous isotropic turbulence. This theory reproduces the decay law $u'^2 \sim t^{-1/2}$ of the linear model of Moffatt (1967) for $N \gg 1$, when the viscous dissipation is neglected. It also yields Kolmogorov's decay law $u'^2 \sim t^{-10/7}$ for $N \ll 1$. However, at intermediate values of N, where both viscous and Joule dissipations are significant, no general power law can be identified.

Regarding the decay of MHD turbulence at low Re_m, there is presently a gap between theoretical results and available experimental data (Moreau, Thess & Tsinober 2007): the first apply to large values of R_λ (the Reynolds number based on the Taylor microscale) and N, while the second are limited to moderate values of both parameters. Further, the present linearized theory strictly refers to the early or final stages of the decay, while empirical data were taken in the initial decay. Numerical simulations are therefore essential to close the gap between different regimes and elucidate the behaviour of decaying MHD turbulence in its entirety. The aim of our study is to provide a detailed analysis of the decay of MHD turbulence. LES in a box with periodic boundaries are performed. Using a sufficiently large box, we minimize the effect of the boundary conditions and achieve a close approximation of homogeneous turbulence. Flows with moderate values of R_λ and fairly large values of N are obtained. Among other results, our study clarifies the apparent contradictions between the experimental observations of Kolesnikov & Tsinober (1972) and the development of the anisotropy, as predicted by the linear theory at large and small scales.

The results presented in the following are valid under the quasi-static approximation and therefore for low magnetic Reynolds numbers. It should be said, however, that our case displays some qualitative similarities with MHD turbulence at high magnetic Reynolds numbers. The latter has been intensively studied in astrophysics and geophysics. For example, the seminal work of Shebalin, Matthaeus & Montgomery (1983), later confirmed by three-dimensional simulations of Oughton, Priest & Matthaeus (1994) and Matthaeus *et al.* (1996), showed that the kinetic energy spectrum becomes anisotropic, with the modes with wave vectors perpendicular to the magnetic field carrying more energy. A second point of contact may be established with dynamos, where the magnetic Reynolds number is moderately large while the magnetic Prandtl number is small. Recent developments have been discussed by Ponty *et al.* (2005) and Mininni (2007). The results reported here could reproduce, admittedly with some simplification, certain features of turbulent dynamos at length scales below the diffusive cut-off scale of the magnetic field.

The paper is organized as follows: after introducing the problem in § 2, the numerical method and the details of the initial conditions are given in § 3. The discussion of the results (§ 4) concerns the kinetic energy (§ 4.1), its dissipation rates (§ 4.2) and the velocity spectra (§ 4.3). Conclusions are summarized in § 5.

2. Problem specification

The evolution of incompressible homogeneous MHD turbulence under the effect of a uniform external magnetic field $\boldsymbol{B}_0$ of intensity B_0 and direction x_3 is described by (see Roberts 1967)

$$\partial_t u_i + u_k \partial_k u_i = -\frac{1}{\rho}\partial_i p + \nu \partial_k^2 u_i - \frac{\sigma B_0^2}{\rho}\partial_k^{-2}\partial_3^2 u_i, \tag{2.1}$$

$$\partial_i u_i = 0. \tag{2.2}$$

Here, $\boldsymbol{u} = (u_1, u_2, u_3)$ is the velocity, p the sum of the kinematic and magnetic pressure, σ the electrical conductivity, ρ the fluid density, ν the kinematic viscosity and ∂_k^{-2} the formal inverse of the Laplacian operator ∂_k^2. It is assumed that the initial flow field has zero mean velocity and shear. In (2.1), the rightmost term is the Lorentz force expressed via the quasi-static approximation. The evolution equation of the Reynolds stress tensor is derived from (2.1) by multiplication by u_j, space averaging and symmetrization

$$\frac{\mathrm{d}}{\mathrm{d}t}\overline{u_j u_i} = -\frac{1}{\rho}\underbrace{\overline{p(\partial_i u_j + \partial_j u_i)}}_{P_{ij}} - \underbrace{2\nu(\overline{\partial_k u_j \partial_k u_i})}_{\epsilon_{\nu_{ij}}} - \underbrace{\frac{\sigma B_0^2}{\rho}\left(\overline{u_j \partial_k^{-2}\partial_3^2 u_i} + \overline{u_i \partial_k^{-2}\partial_3^2 u_j}\right)}_{\epsilon_{J_{ij}}}. \tag{2.3}$$

Hereafter, summation is implied over the same index (unless otherwise stated), the overbar denotes averaging over the homogeneous directions and the explicit time dependence is dropped most of the times. The three tensors P_{ij}, $\epsilon_{\nu_{ij}}$ and $\epsilon_{J_{ij}}$ represent the effect of the pressure–rate-of-strain correlation, viscous dissipation and Joule dissipation. The trace of (2.3) yields the equation for the turbulent kinetic energy $K = \overline{u_i u_i}/2$, i.e.

$$\frac{\mathrm{d}}{\mathrm{d}t}\underbrace{\frac{1}{2}\overline{u_i u_i}}_{K} = -\underbrace{\nu(\overline{\partial_k u_i \partial_k u_i})}_{\epsilon_\nu} - \underbrace{\frac{\sigma B_0^2}{\rho}\left(\overline{u_i \partial_k^{-2}\partial_3^2 u_i}\right)}_{\epsilon_J}. \tag{2.4}$$

Thus, the temporal decay of K is due to the Joule dissipation rate ϵ_J and the viscous dissipation rate ϵ_ν. The latter can be equivalently expressed by

$$\epsilon_\nu = 2\nu\overline{s_{ij}s_{ij}} = \tfrac{1}{2}\nu\overline{(\partial_j u_i + \partial_i u_j)^2}, \tag{2.5}$$

where $s_{ij} = 1/2(\partial_j u_i + \partial_i u_j)$ is the fluctuating rate-of-strain tensor (e.g. Pope 2000).

The kinetic energy budget in spectral space is

$$\partial_t \Phi_{ij}(\boldsymbol{k}) = T_{ij}(\boldsymbol{k}) - 2\left(\nu k^2 + \frac{\sigma B_0^2}{\rho}\frac{k_3^2}{k^2}\right)\Phi_{ij}(\boldsymbol{k}), \tag{2.6}$$

where $\Phi_{ij}(\boldsymbol{k})$ is the spectral tensor (e.g. Batchelor 1967), related to the ensemble average of the product $\hat{u}_i(\boldsymbol{k})\hat{u}_j^*(\boldsymbol{k})$. Here, the hat represents the Fourier transform, the asterisk denotes (here only) complex conjugate and $\boldsymbol{k}$ is the wavenumber vector of modulus k. $T_{ij}(\boldsymbol{k})$ is the nonlinear transfer tensor and $k_3^2/k^2 = \cos^2(\psi)$, with ψ being the angle between $\boldsymbol{B}_0$ and $\boldsymbol{k}$. From (2.6), it is clear that if $\Phi_{ij}(\boldsymbol{k})$ is initially a diagonal tensor (in a suitably chosen frame of reference), it remains so at all times. This is analogous to initially isotropic turbulence subject to rotation: the off-diagonal components of Φ_{ij} remain zero, while its normal components are being redistributed (e.g. Mathieu & Scott 2000).

From the shell average of $\Phi_{ii}(\boldsymbol{k})$, one obtains the three-dimensional spectrum of the kinetic energy:

$$E(k) = k^2 \int_0^{\pi} \int_0^{2\pi} \Phi_{ii}(k, \varphi, \psi)\, \mathrm{d}\varphi \sin(\psi)\, \mathrm{d}\psi, \tag{2.7}$$

where (k, φ, ψ) are the variables in the spherical coordinate system in spectral space; the three-dimensional spectrum $E_i(k)$ of the ith component can be derived similarly. Plane averaging of Φ_{ii} yields one-dimensional spectra. For example, for $i = 1$,

$$\phi_{11}(k_1) = \int\!\!\int_{-\infty}^{\infty} \Phi_{11}(k_1, k_2, k_3)\, \mathrm{d}k_2\, \mathrm{d}k_3. \tag{2.8}$$

Note that

$$\frac{\overline{u_1 u_1}}{2} = \int_0^{\infty} E_1(k)\, \mathrm{d}k = \int_0^{\infty} \phi_{11}(k_1)\, \mathrm{d}k_1, \tag{2.9}$$

and

$$\epsilon_{\nu 1} = 2\nu \int_0^{\infty} k^2 E_1(k)\, \mathrm{d}k. \tag{2.10}$$

The importance of the last term in (2.1) with respect to inertia is quantified by the magnetic interaction parameter

$$N = \frac{\sigma B_0^2}{\rho} \frac{L}{(2K/3)^{1/2}}, \tag{2.11}$$

where

$$L = \frac{3\pi}{4K} \int_0^{\infty} \frac{E(k)}{k}\, \mathrm{d}k \tag{2.12}$$

is the integral length scale. As in other works (e.g. Schumann 1976; Zikanov & Thess 1998; Vorobev *et al.* 2005), in (2.11) L is estimated from the isotropic flow, before applying $\boldsymbol{B}_0$. In homogeneous anisotropic turbulence, it is also useful to define the one-dimensional integral length scale (e.g. Mathieu & Scott 2000, p. 273):

$$L_i = \frac{\pi}{\overline{u_i^2}} \phi_{ii}(k_i = 0) \tag{2.13}$$

(no implied summation here); in HIT, $L \equiv L_i$. Note that, in the literature (e.g. Pope 2000), the one-dimensional spectrum is sometimes defined as $\phi_{11}^{[1]} = 2\phi_{11}$, and therefore there is a factor 2 in the denominator of L_i. The interaction parameter can also be expressed as the ratio

$$N = T/\tau \tag{2.14}$$

of the eddy turnover time

$$T = \frac{L}{(2K/3)^{1/2}} \tag{2.15}$$

to the magnetic damping time

$$\tau = \frac{\rho}{\sigma B_0^2}. \tag{2.16}$$

In the following, the asterisk indicates normalization of time by T. The turbulence intensity can be quantified by the Taylor microscale Reynolds number:

$$R_\lambda = \sqrt{\frac{15}{\nu \epsilon_\nu}} \frac{2K}{3}. \tag{2.17}$$

Schumann (1976) suggested that, instead of R_λ, the Reynolds number based on the integral length scale L

$$R_L = \frac{(2K/3)^{1/2} L}{\nu} \tag{2.18}$$

should be considered. This approach is justified, since the large scales substantially contribute to the Joule dissipation, which strongly affects the decay when N is large. Without magnetic field, Schumann (1976) had $R_L = 60$ and $R_\lambda = 43$. Alemany *et al.* (1979) provided the Reynolds number based only on the mesh size:

$$R_M = \frac{u' M}{\nu}, \tag{2.19}$$

where u' was extrapolated to the virtual origin of the grid. In the experiment, R_M ranged from 750 to 9000. In order to estimate the corresponding value of R_λ, one can assume that $L\,(t=0) \simeq M$ and that the kinetic energy dissipation rate coefficient

$$C_\epsilon = \frac{\epsilon_\nu L}{u'^3} \tag{2.20}$$

is equal to 1. The result is that

$$R_\lambda = \sqrt{\frac{15}{\nu \epsilon_\nu}} u'^2 = \sqrt{\frac{15 L u'}{\nu C_\epsilon}}, \tag{2.21}$$

or

$$R_\lambda = \sqrt{15 R_M}, \tag{2.22}$$

which yields values ranging from 106 to 367.

Before presenting our numerical results, it is worth recalling a few known features of the damping mechanism in MHD turbulence. Let us consider the spectral form of the Joule dissipation in (2.6):

$$2\frac{\sigma B_0^2}{\rho} \cos^2(\psi)\, \Phi_{ij}(\boldsymbol{k}). \tag{2.23}$$

Since the coefficient in front of $\Phi_{ij}(\boldsymbol{k})$ is independent of the wavenumber k, the bulk of Joule dissipation corresponds and applies to the energy containing range of scales. Unlike the small scales, which require the development of the energy cascade, the large scales are present at the beginning of the decay and so is the magnetic damping. It is also evident from (2.23) that Joule dissipation is larger for small values of ψ. As a result, one expects that the turbulent energy would be selectively depleted from the region near the k_3 axis, parallel to the magnetic field. Following this reasoning, Sommeria & Moreau (1982) conjectured that for $N \gg 1$ and at the dynamical equilibrium, the turbulent energy would concentrate outside the cone defined by $\psi = \pi/2 - N^{-1/2}$. Although this picture may be overly simplified, it nonetheless suggests that as N increases, the dependence of the velocity field on the k_3 direction is attenuated, possibly leading to a two-dimensional velocity field (Alemany *et al.* 1979).

Much less is known about the other type of anisotropy, that between the velocity components (i.e. in terms of the Reynolds stress tensor). The development of this anisotropy during the entire decay has never been documented. Moffatt's (1967) result provides an answer that applies only to the linear regime for $N \gg 1$. His derivation is repeated here, as it will be useful in the following. From (2.6), by neglecting the nonlinear and viscous terms, one has

$$\partial_t \Phi_{ii}(\boldsymbol{k},t) \doteq -\frac{2}{\tau}\cos^2(\psi)\,\Phi_{ii}(\boldsymbol{k},t) \tag{2.24}$$

(no implied summation here) whose solution is

$$\Phi_{ii}(\boldsymbol{k},t) \doteq \Phi_{ii}(\boldsymbol{k},0)\exp\left(-2\cos^2(\psi)\frac{t}{\tau}\right). \tag{2.25}$$

By hypothesis, the initial velocity field $\hat{u}_i(\boldsymbol{k},0)$ is isotropic and therefore its spectral tensor can be written as

$$\Phi_{ij}(\boldsymbol{k},0) = \frac{E(k,0)}{4\pi k^2}\left(\delta_{ij} - \frac{k_i k_j}{k^2}\right). \tag{2.26}$$

In particular, the parallel and perpendicular components are (Schumann 1976)

$$\Phi_{\parallel}(\boldsymbol{k},0) = \frac{E(k,0)}{4\pi k^2}\sin^2(\psi), \tag{2.27}$$

$$\Phi_{\perp}(\boldsymbol{k},0) = \frac{E(k,0)}{4\pi k^2}\frac{1}{2}[1+\cos^2(\psi)]. \tag{2.28}$$

(Hereafter, a quantity in the direction parallel to $\boldsymbol{B}_0$ is denoted by the subscript $\parallel$, while the subscript $\perp$ indicates the average of the same quantity along the other two directions.) By virtue of (2.25), integration of $\Phi_{\parallel}(\boldsymbol{k},t)$ and $\Phi_{\perp}(\boldsymbol{k},t)$ yields

$$\frac{\overline{u_{\parallel}^2}(t/\tau)}{\overline{u_{\perp}^2}(t/\tau)} \doteq \frac{\displaystyle\int_0^{\pi}\sin^3(\psi)\exp\left[-2\cos^2(\psi)\frac{t}{\tau}\right]\mathrm{d}\psi}{\displaystyle\int_0^{\pi}\tfrac{1}{2}\left[1+\cos^2(\psi)\right]\sin(\psi)\exp\left[-2\cos^2(\psi)\frac{t}{\tau}\right]\mathrm{d}\psi}, \tag{2.29}$$

independently of the initial energy spectrum $E(k,0)$. For $t/\tau \gg 1$ (but $t/T \ll 1$ for the linear approximation in (2.24) to be valid), one obtains

$$K_{\parallel} = 2K_{\perp}. \tag{2.30}$$

Moffatt (1967) refers to this as the channelling of the kinetic energy into the parallel velocity component.

3. Numerical method and initial conditions

Equations (2.1) and (2.2) are solved in a domain with periodic boundary conditions using the LES approach. Details of the method are given in Knaepen, Kassinos & Carati (2004) and only a brief description is provided here. The nonlinear term is evaluated in physical space while the other terms in Fourier space; aliasing errors are removed using the 2/3 algorithm. Time advancement is performed with a third-order, low-storage Runge–Kutta integration scheme (Williamson 1980). The effect of the small scales on the resolved field is accounted via the Smagorinsky method using the dynamic procedure of Germano *et al.* (1991), as modified by Lilly (1992),

Cases	Resolution	$\mathscr{L}_1 \times \mathscr{L}_2 \times \mathscr{L}_3$	$R_\lambda(0)$	R_L	$S_i(0)$	C_ϵ
$N = 0, 0.5, 1, 3$	$128 \times 128 \times 128$	$2\pi \times 2\pi \times 2\pi$	170	1000	−0.44	0.49
$N = 0, 10, 50$	$128 \times 128 \times 512$	$2\pi \times 2\pi \times 8\pi$	168	985	−0.45	0.47

TABLE 1. Main properties at initial conditions (zero magnetic field). In all cases, the viscosity ν is 0.0003.

in order to determine the volume-averaged Smagorinsky constant C at each time step. In previous work (Knaepen & Moin 2004; Knaepen *et al.* 2004; Vorobev *et al.* 2005), it was verified with the help of DNS data that the dynamic model accurately describes MHD turbulence. Under the quasi-static approximation, the Lorentz force is a linear function of the velocity and therefore commutes with the LES filtering. As a consequence, this approach does not require explicit modelling of the effect of the magnetic field on the subgrid-scale term. The viscous dissipation rate ϵ_ν is given by the sum of the contributions from the resolved velocity field ϵ_r and the unresolved subgrid-scale motion ϵ_s, i.e.

$$\epsilon_\nu = \epsilon_r + \epsilon_s. \tag{3.1}$$

Table 1 lists the main flow properties at the initial state. In addition to HIT (i.e. $N = 0$), five values of N are considered. The initial velocity field computed for $N = 0$ is used for all runs. In order to closely replicate the experimental conditions of Alemany *et al.* (1979), the magnetic field is applied directly to the initialized velocity field, without a preliminary period of decay. In the experiment, the grid was dragged within the region of fluid surrounded by the magnet.

The numerical domain is either a cube or, for the cases with larger N, a parallelepiped with the dimension ($\mathscr{L}_3$) in the direction of $\boldsymbol{B}_0$ four times larger than the other dimensions ($\mathscr{L}_1$, $\mathscr{L}_2$). This stretching allows longer runs, before the assumption of periodic boundaries becomes questionable due to the preferential elongation of the turbulent structures in the direction of $\boldsymbol{B}_0$. In all cases, the small-scale resolution is unchanged. The importance of an adequate resolution of the energy containing range and the effect of the boundary condition in the decay of HIT was underlined by Wang & George (2002) and other authors. In particular, Pope (2000) suggested that for the periodic boundary conditions to be a valid approximation, L should be less than $\mathscr{L}/8$. In the present anisotropic case, $L_\parallel$ approaches the box size $\mathscr{L}_\parallel = \mathscr{L}_3$ before $L_\perp$ nears $\mathscr{L}_\perp = \mathscr{L}_1 = \mathscr{L}_2$, and therefore we safely impose that $\max(L_\parallel) \leqslant \mathscr{L}_\parallel/10$.

In table 1, $C_\epsilon = \epsilon_\nu L/u'^3$ is the dissipation-rate coefficient. Its value is close to 0.5, consistent with the present value of $R_\lambda(0)$ (e.g. Burattini, Lavoie & Antonia 2005). The velocity derivative skewness

$$S_i = \frac{\overline{(\partial_i u_i)^3}}{\overline{(\partial_i u_i)^2}^{3/2}} \tag{3.2}$$

(no implied summation here), which is a signature of the nonlinear term, is initially equal to −0.44. This is obtained by allowing a preliminary iterative correlation of the phases of the Fourier modes. The procedure consists of computing the nonlinear term, advancing the solution and rescaling back the velocity field to the initial spectrum. Without this procedure, the initial Smagorinsky constant is zero and the flow takes longer to achieve the canonical decay.

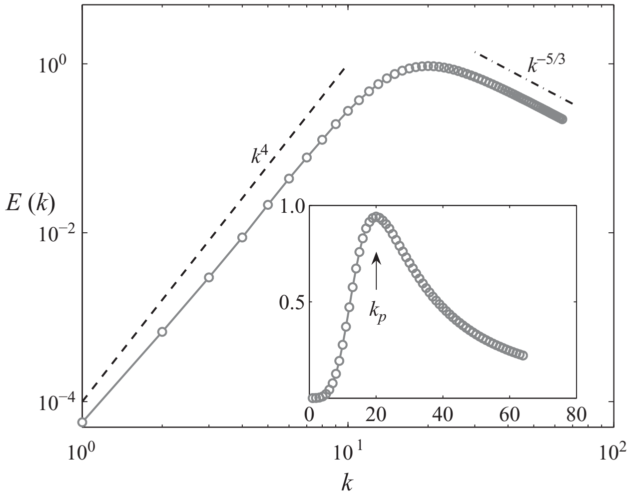

FIGURE 1. Initial velocity spectrum, as defined by (3.3). Inset: spectrum plotted in linear scales.

The initial velocity spectrum is defined by

$$E(k,0) = k^{-5/3}\left[\frac{kL}{\left[(kL)^4 + C_L\right]^{1/4}}\right]^{5/3+p_0}, \tag{3.3}$$

where p_0 (=4) is the slope at low k, the exponent $-5/3$ accounts for the inertial range and

$$C_L = \left[C_K \int_0^\infty \frac{y^{p_0}}{[y^4+1]^{5/12+p_0/4}}\mathrm{d}y\right]^6 \tag{3.4}$$

follows from the definition of the integral scale (2.12). In (3.4), $C_K = 1.5$ is the Kolmogorov constant and y is a dummy integration variable. The distribution of (3.3), plotted in figure 1, is a slight modification of that in Pope (2000), the former having a faster transition between the k^4 and the $k^{-5/3}$ regime. From (3.3), the maximum of the spectrum (3.3) is at the wavenumber

$$k_p = \frac{1}{L}\sqrt[4]{\frac{3}{5}p_0 C_L} = 20. \tag{3.5}$$

See the inset of figure 1.

4. Results

4.1. *Turbulent kinetic energy*

Figure 2 reports the decay of K at different values of N. For the hydrodynamic case, the profile is rather flat until, for $t^* \gtrsim 1$, viscous dissipation starts acting at the small scales that are populated through the cascade. Compared to $N = 0$, the primary effect of $\boldsymbol{B}_0$ is to shift the beginning of decay to an earlier time, especially at the largest values of N. This is due to the Joule dissipation, which acts immediately at all scales. Despite early differences, the distributions with $\boldsymbol{B}_0 \neq 0$ tend to converge at large times.

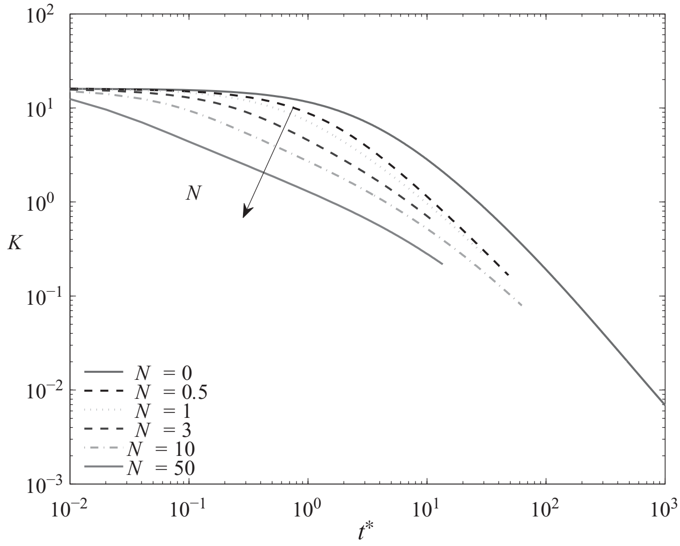

FIGURE 2. Decay of the turbulent kinetic energy at different values of the interaction parameter.

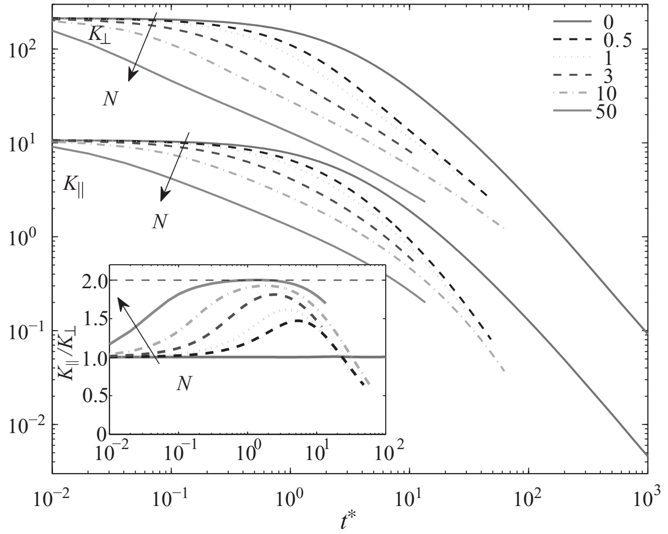

FIGURE 3. Decay of the turbulent kinetic energy of the parallel and perpendicular velocity components. Distributions of $K_\perp$ are shifted upwards by 20 units. Inset: ratios of the kinetic energy components.

In § 1, we noted that available experiments reported the decay of either $K_\parallel$ or $K_\perp$. Figure 3 shows that for any given value of N, the profile of $K_\parallel$ differs substantially from that of $K_\perp$. The relative importance of the two components of K varies in time, with $K_\parallel$ and $K_\perp$ respectively being the largest contributors of K during the early and late stages. This is illustrated in the inset of figure 3, which shows $K_\parallel/K_\perp$. The ratio is bounded from above by the value of 2. Such limit, which corresponds to the prediction of the linear model of Moffatt (1967) (see (2.30)), is attained only

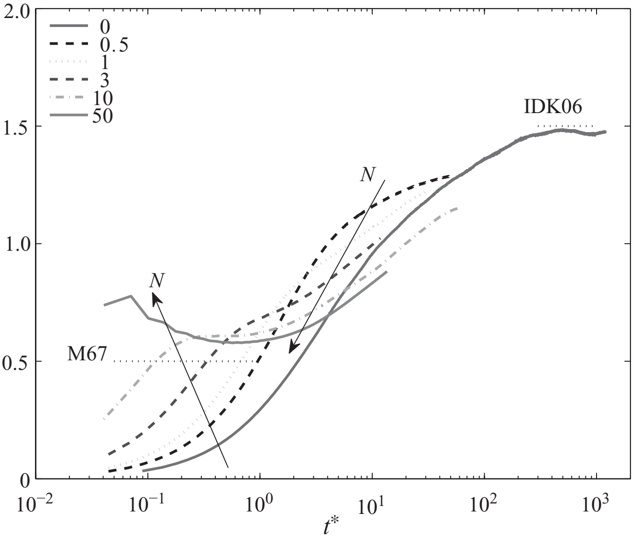

FIGURE 4. Logarithmic derivative of K. IDK06 ($m = 1.5$) is the value computed by Ishida *et al.* (2006); M67 (horizontal dashed line at $m = 1/2$) is the value predicted by Moffatt (1967).

for $N = 50$, albeit briefly. The anisotropy of the Reynolds stress tensor is further discussed in § 4.1.2. It is worth noting that Matthaeus *et al.* (1996), who performed simulations of full MHD turbulence, showed that $K_{\perp}$ exceeds $K_{\parallel}$ at a late stage of the decay, although only for a compressible flow.

Some parts of the curves in figures 2 and 3 seemingly display a linear trend. This implies the establishment of a power law of the type

$$K = (t - t_0)^{-m}, \tag{4.1}$$

where m (>0) is the decay exponent and t_0 the virtual origin. It should be stressed at the outset that although such conclusion is supported by earlier experimental evidence (Kolesnikov & Tsinober 1972; Alemany *et al.* 1979), it is not derivable analytically for intermediate values of N – that is, when both viscous and magnetic dissipation rates are not negligible. As remarked in § 1, in the limit cases of $N \gg 1$ and $N \ll 1$ one can respectively use the linear theory of Moffatt (1967) with $m = 1/2$ (but only for $\tau < t < T$) and the data collected for the pure hydrodynamic case.

The validity of (4.1) in our numerical experiment is verified directly by assuming $t \gg t_0$ and estimating the logarithmic derivative

$$m(t) = -\frac{\mathrm{d}\ln(K)}{\mathrm{d}\ln(t)} = -\frac{t}{K}\frac{\mathrm{d}K}{\mathrm{d}t}. \tag{4.2}$$

If K decays according to a power law over a certain time interval, then the profile of $m(t)$ displays a plateau. This procedure is more reliable than fitting linearly a curve to the data over an arbitrary range. Distributions of m computed via (4.2) are plotted in figure 4. After an early phase, the curve for $N = 0$ levels off near 1.5. This value is in close agreement with that of Ishida *et al.* (2006), who performed DNS at high resolution using, like here, an initial spectrum with a k^4 power law at low wavenumbers. For the MHD cases, the decay rate is initially larger than in the hydrodynamic case. For $N = 10$ and 50 and within one eddy turnover time, m displays

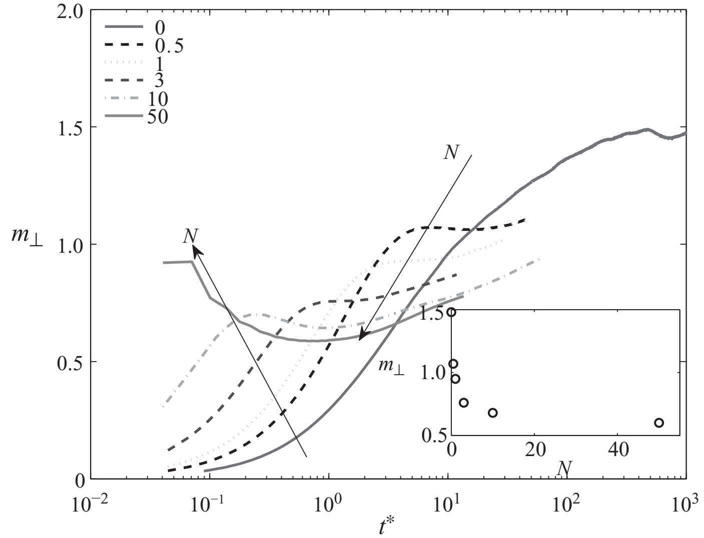

FIGURE 5. Logarithmic derivative of $K_\perp$. Inset: estimate of the decay exponents in the plateau region as a function of N.

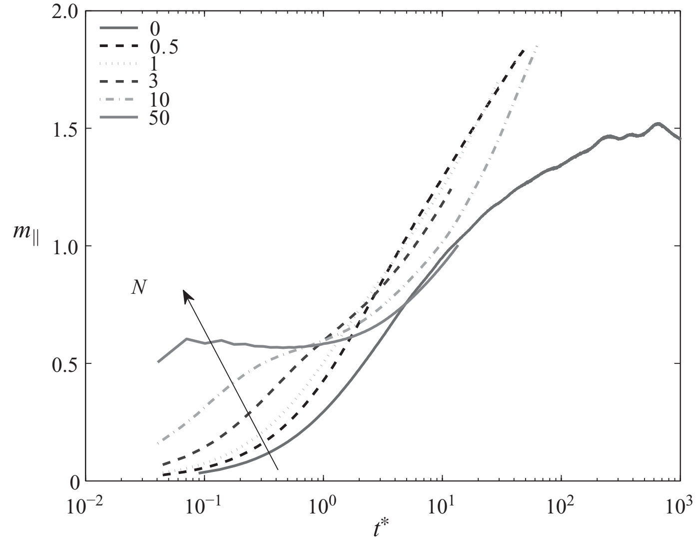

FIGURE 6. Logarithmic derivative of $K_\parallel$.

a first plateau at $m \simeq 0.6$, slightly exceeding 1/2 of the linear theory. For lower values of N, the curves tend to level off only later and at larger values of m. At later stages, approximately for $t^* \gtrsim 1$ the decay rate decreases with increasing magnetic field. Such slowdown of the decay is similar to that imposed on homogeneous turbulence by rigid rotation, although in this case there is no additional dissipation (e.g. Mathieu & Scott 2000; Yu, Girimaji & Luo 2005).

As observed above, in any single previous experiment either $K_\parallel$ or $K_\perp$ was measured. Therefore, it is useful to examine the decay exponents $m_\parallel$ and $m_\perp$ of the individual velocity components. The results are presented in figures 5 and 6. For $N = 50$, both sets of curves display the first plateau at $m \simeq 0.6$. As N decreases, the regions of

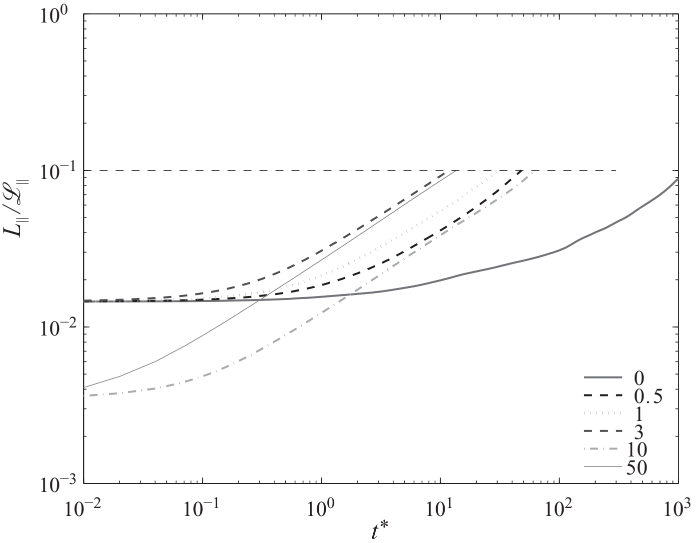

FIGURE 7. Integral length scale from the parallel velocity component. Horizontal dashed line marks a tenth of the box size in the parallel direction $\mathscr{L}_\parallel$. The curves for $N = 10$ and 50 start from a lower point due to the larger box size in the parallel direction.

power law of $K_\parallel$ disappear, while the power-law behaviour of $K_\perp$ becomes more evident at later times (estimates of $m_\perp$ in this regime are plotted in the inset of figure 5). From figures 5 and 6, one noteworthy observation can be made: at later times the decay rate of $K_\parallel$ is consistently larger than that of $K_\perp$. This inequality reconciles the observations of Alemany *et al.* (1979) and Kolesnikov & Tsinober (1972). The first experiment provided $m_\parallel = 1.7$ ($m = 1$ at $N = 0$) for $8 \leqslant x/M \leqslant 20$, while the second experiment $m_\perp = 0.23$ ($m = 1.4$ at $N \simeq 0$) for $2.5 \leqslant x/M \leqslant 40$. (Kolesnikov & Tsinober's (1972) values have been estimated from their figures). While these values do not precisely match those calculated here, and admittedly $K_\parallel$ does not follow a power-law decay, our results nevertheless confirm that $K_\perp$ decays at a significantly slower rate than $K_\parallel$. This suggests that the differences between $m_\parallel$ and $m_\perp$ are intrinsic to this homogeneous flow, and that wall effects are not essential in order to explain the discrepancies between the two experiments.

4.1.1. *Integral length scales*

Figures 7 and 8 show the temporal profiles of the parallel $L_\parallel$ and perpendicular $L_\perp$ integral length scales. The monotonic growth of $L_\parallel$ compared to the rather flat behaviour of $L_\perp$ signifies that, as demonstrated in earlier computational and theoretical studies, the large-scale structures elongate in the direction of $\boldsymbol{B}_0$. The effect is quantified by the ratio $L_\parallel/L_\perp$ (see the inset of figure 8). Note that, before increasing, $L_\perp$ initially decreases slightly. Davidson (1997) remarked that in the linear-theory framework, the validity of $K \sim t^{-1/2}$ implies that $L_\parallel/L_\perp \sim t^{1/2}$. This prediction, which has never been corroborated by experiments, is tested in figure 9. At large N and for $t^* < 1$, the logarithmic derivative $\mathrm{d}\left[\ln\left(L_\parallel/L_\perp\right)\right]/\mathrm{d}\left[\ln(t)\right]$ indeed approaches the value 1/2. It is worth noting that if one considered the slope of only $L_\parallel$, the exponent 1/2 would be attained at even lower values of N and over a wider time interval, as shown in the inset of figure 9.

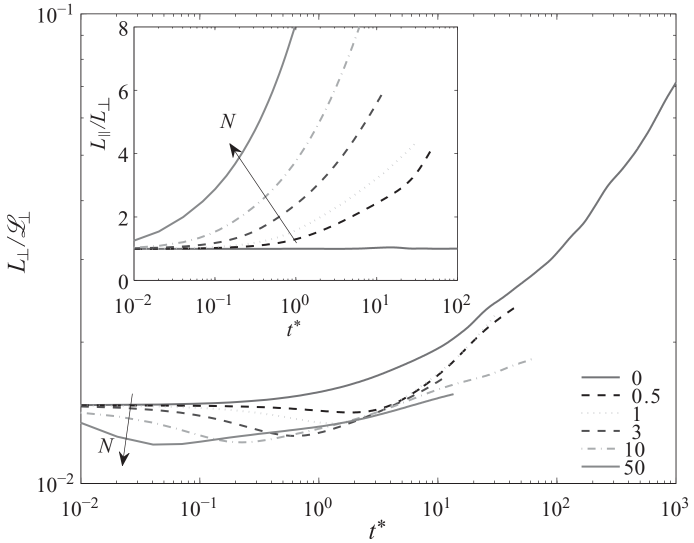

FIGURE 8. Integral length scale from the perpendicular velocity component. Inset: ratio of the integral length scales.

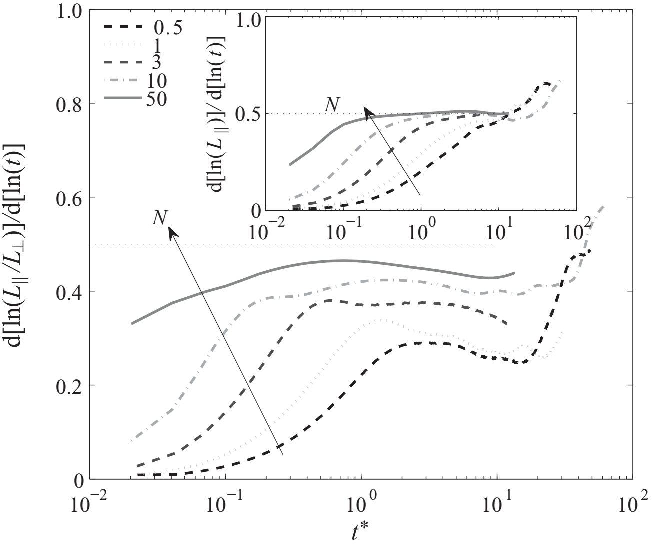

FIGURE 9. Logarithmic derivative of the ratio of the integral length scales. The horizontal dotted line at 1/2 corresponds to the result of Moffatt (1967). Inset: logarithmic derivative of the parallel integral length scale.

The elongation of the turbulent structures is further illustrated in figure 10, which reports the spatial distribution of the kinetic energy for $N = 0.5$. At $t^* = 0$, the contours are isotropic, while at $t^* = 8.8$, and even more at $t^* = 32$, the fluctuations are elongated in the direction of $\boldsymbol{B}_0$. Note that the dimensional anisotropy of the integral length scales occurs at significantly earlier times than the anisotropy of the kinetic energy components. For example, at $t^* = 32$ one has $L_\parallel/L_\perp = 3.6$, while $K_\parallel/K_\perp = 0.84$.

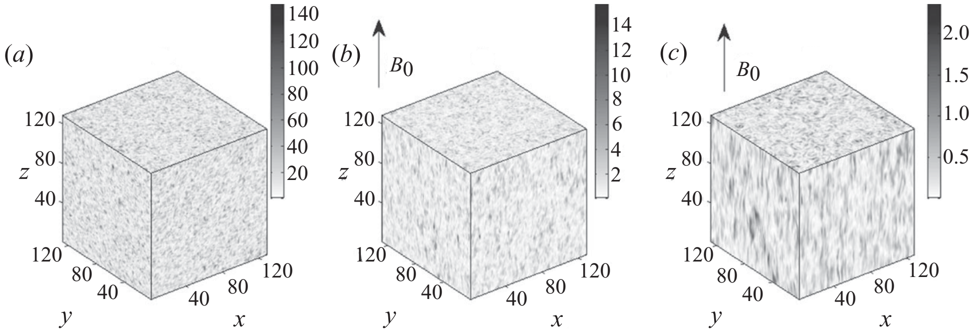

FIGURE 10. Contours of the kinetic energy for $N = 0.5$. (*a*) $t^* = 0$; (*b*) $t^* = 8.8$; (*c*) $t^* = 32$.

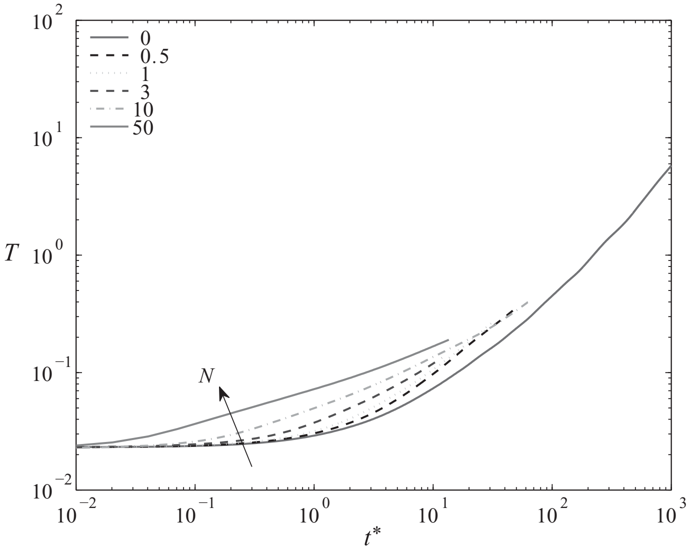

FIGURE 11. Profiles of the eddy turnover time defined with the integral length scale $L_\perp$.

The temporal profiles of the eddy turnover time are shown in figure 11. According to (2.14), this can also be interpreted as the instantaneous value of the interaction parameter. In this sense, it is apparent that the effect of the magnetic field compared to inertia becomes stronger over time. As is the case for K, the curves of the MHD runs tend to converge, as t^* grows.

4.1.2. *Anisotropy invariants*

Here, we consider the type and degree of the large-scale anisotropy of the velocity components. This is quantified by the Reynolds stress anisotropy tensor

$$b_{ij} = \frac{\overline{u_i u_j}}{\overline{u_i u_i}} - \frac{1}{3}\delta_{ij}, \tag{4.3}$$

where δ_{ij} is the Kronecker delta. It is traceless by construction and has two non-trivial invariants: $II = -b_{ij}b_{ji}/2$ and $III = b_{ij}b_{jk}b_{ki}/3$, the latter being the determinant of b_{ij} (Pope 2000; Choi & Lumley 2001). Because of the definition (4.3), throughout the decay it holds that $b_\parallel = -2b_\perp$, where $b_\parallel = b_{33}$ and $b_\perp = (b_{11} + b_{22})/2$. As shown in figure 12, $b_\parallel$ is initially positive and increasing, but after having attained a maximum,

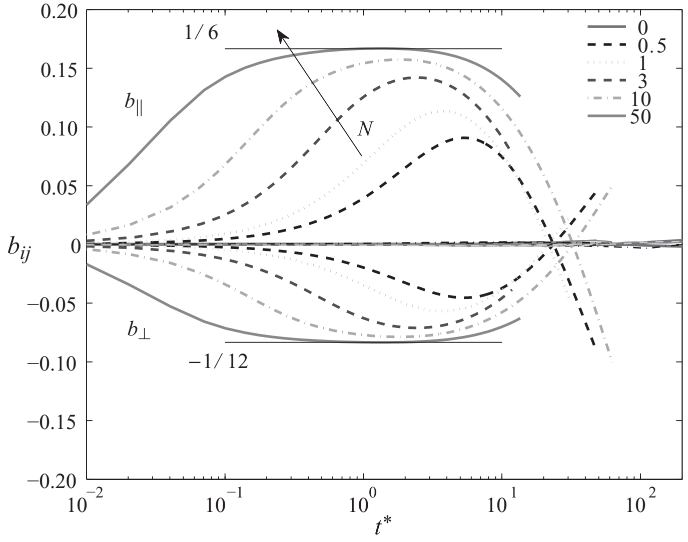

FIGURE 12. Components $b_\parallel$ and $b_\perp$ of the Reynolds stress anisotropy tensor. The distributions of b_{ij} for $i \neq j$ are $\simeq 0$.

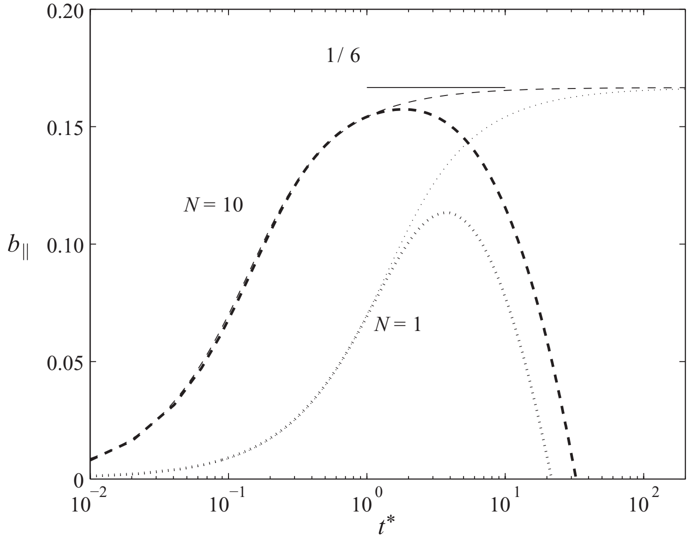

FIGURE 13. Comparison of the temporal profile of $b_\parallel$ from the analytical solution (2.29) (thin lines) and from the numerical data (thick lines).

it decreases and becomes negative. Note that as N increases, the maximum of $b_\parallel$ approaches the limit $b_{\parallel\infty} = 1/6$, corresponding to $K_\parallel = 2K_\perp$, which follows from the linear model of Moffatt (1967). As discussed above, this stage of the decay is identifiable with the power-law behaviour with exponent 1/2. When $N = 50$, the numerical solution attains this limit, but for lower values of N, max $(b_\parallel)$ is a fraction of $b_{\parallel\infty}$. This is further highlighted in figure 13, where the numerical data are compared to the analytical solution, as per (2.29). For $N = 10$, the two curves are close, up to

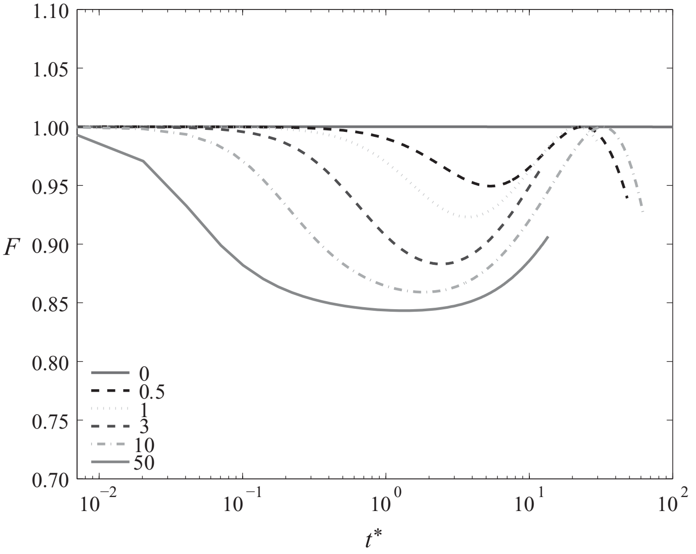

FIGURE 14. Evolution of the anisotropy factor F of the Reynolds stresses; see (4.4).

almost the asymptotic value. For $N = 1$, however, the development of the anisotropy is slower in the simulation and the nonlinear effects keep $b_\parallel$ away from the asymptote.

From the second and third invariants of b_{ij}, one can define the scalar function

$$F = 1 + 27III + 9II, \tag{4.4}$$

which is an indicator of the large-scale anisotropy (Choi & Lumley 2001); F vanishes when the Reynolds stress tensor becomes two-dimensional and is unity for isotropic conditions (e.g. Pope 2000). The profiles of F in figure 14 have a local minimum, corresponding to max $\left(b_\parallel\right)$, followed by a maximum. Each such maximum implies a temporary isotropic state with $b_\parallel \simeq b_\perp \simeq 0$ (see figure 12). At low N, the maxima are achieved at $t^* \simeq 25$. However, this condition of isotropy pertains only the kinetic energy components, since the integral length scales $L_\parallel$ and $L_\perp$ are rather disproportionate at this point in time (figure 8). One should therefore be careful in deducing properties of the velocity field from the shape of the turbulent structures.

The type of anisotropy of the Reynolds stress tensor can be quantified by the anisotropy invariant map (AIM). The map illustrates the path of the variables (η, ξ), which are related to the invariants by $\eta^2 = -II/3$ and $\xi^3 = III/2$; η and ξ respectively represent the degree and type of the anisotropy. All the possible states of turbulence are confined inside the Lumley triangle (e.g. Choi & Lumley 2001). On the triangle's left side, turbulence is axisymmetric and the shape of the Reynolds stress ellipsoid is disc-like, with one component of the turbulent kinetic energy smaller than the other two. On its right side, turbulence is also axisymmetric but the ellipsoid is rod-shaped, as one component of K is larger than the other two. Figure 15 shows that turbulence is rod-shaped during the first phase of the decay. The rightmost location of (η, ξ) – which corresponds to max $\left(b_\parallel\right)$ in figure 12 – moves further left with increasing N, but is limited by the values of the linear theory

$$\eta_\infty = \left(b_{ii}^2/6\right)^{1/2} = (2^2 \times 3)^{-1}, \tag{4.5}$$

$$\xi_\infty = \left(b_{ii}^3/6\right)^{1/3} = (2^2 \times 3)^{-1} = \eta_\infty. \tag{4.6}$$

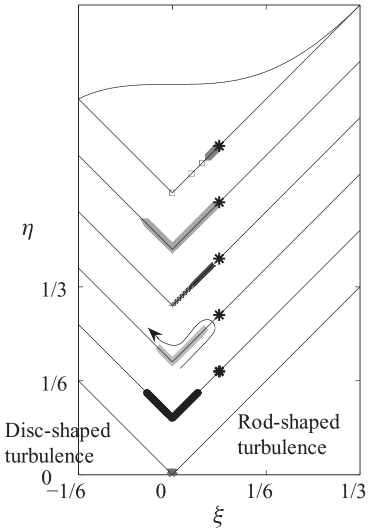

FIGURE 15. AIM of Reynolds stresses. $N = 0$ (values are in the origin), $N = 0.5$, 1, 3, 10, 50 (each shifted progressively upwards by 0.1). The arrow indicates the direction of the path; asterisks denote the limit η_∞, ξ_∞.

After having reached the extremum, the flow state moves back towards the origin (the isotropic condition), and finally follows the other straight side of the triangle, where the Reynolds stress ellipsoid is disc-shaped (although the turbulent structures are elongated). The final position on this triangle's side is imposed by the computational constraint on $L_\parallel$, and it seems plausible that – if the size of the box were large enough – the flow would reach the two-dimensional state. Vorobev *et al.* (2005) conducted a similar analysis of MHD turbulence with large-scale forcing. Contrary to the present values of (η, ξ), which precisely follow the borders of the triangle, theirs were rather scattered throughout the lower portion of the triangle. Most likely, this was due to the forcing, which introduced some shear. As a consequence, no conclusion could be drawn regarding the anisotropy of the large scales.

4.2. *Mean dissipation rates*

In this section, we consider the viscous and Joule dissipation rates, which, according to (2.4), determine the decay of kinetic energy. The component due to viscosity (given by the sum of the resolved plus subgrid-scale contributions) is plotted in figure 16. Again, as N increases, the decay starts earlier so that, over the longer period, ϵ_ν is smaller. For the time interval considered, the ratio $\epsilon_{\nu\parallel}/\epsilon_{\nu\perp}$ is always >1 (inset of figure 16). Therefore, in the initial phase, $u_\parallel$ has a larger amplitude not only at large scales (figure 3) but also at small scales. Eventually, $\epsilon_{\nu\parallel}/\epsilon_{\nu\perp}$ decreases, when the fluctuations of the parallel velocity field are more damped by the magnetic field.

We have already pointed out that of the kinetic energy components, $K_\perp$ displays the clearest power law (figure 5). Therefore, the following analysis of the power-law behaviour is limited to $\epsilon_{\nu\perp}$. The results are presented in figure 17. For $N = 0$, one can see that $m_\nu = m + 1 \simeq 2.5$, which is expected, since K follows a power law and the kinetic energy budget yields $\epsilon_\nu \sim t^{-m-1}$. For $N \neq 0$, $m_{\nu\perp}$ also displays a plateau at values that decrease with N, as was the case for $m_\perp$ in figure 5. Significantly, the relation $m_{\nu\perp} \simeq m_\perp + 1$ still holds, to a good approximation.

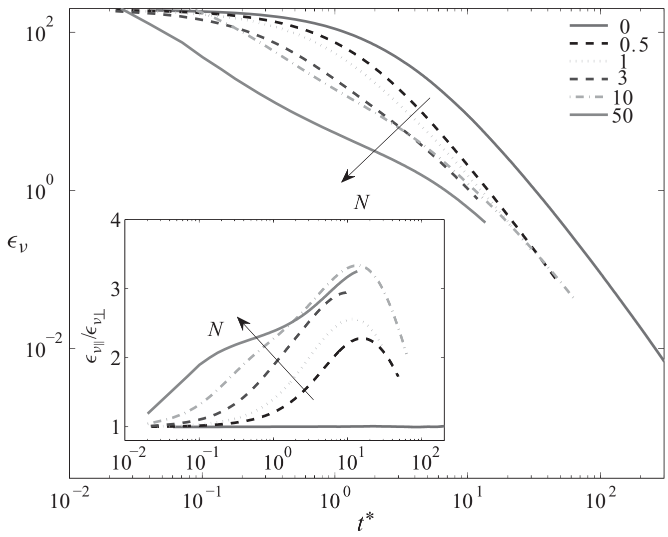

FIGURE 16. Profile of the viscous dissipation rate. Inset: ratio of the viscous dissipation components.

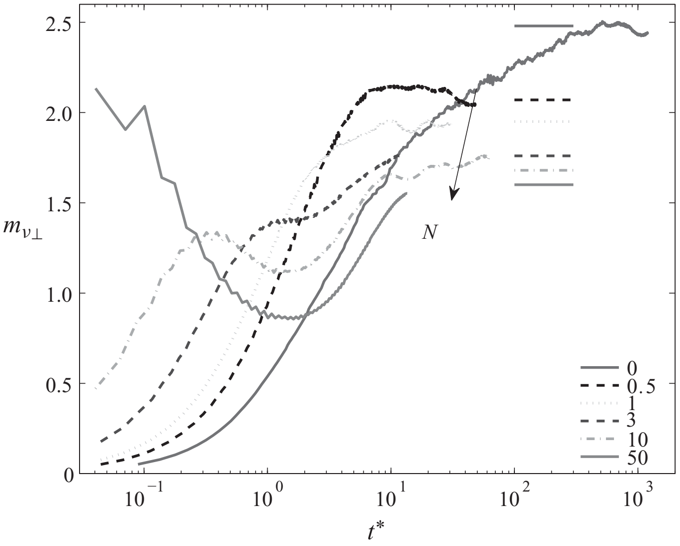

FIGURE 17. Decay exponent of the perpendicular component of the viscous dissipation rate. Horizontal lines in the upper right corner are at $m_\perp + 1$, with $m_\perp$ estimated from the second plateau of figure 5.

As illustrated in figure 18, the relative contributions of the subgrid-scale ϵ_s and resolved ϵ_r motions to the viscous dissipation rate change significantly during the decay. The first contribution, which is much larger at the beginning, eventually becomes smaller than the second. Furthermore, the increase of the magnetic field leads to a reduction of ϵ_r, in connection to the small-scale damping. In response to the flow evolution, the dynamical model adapts the Smagorinsky constant (inset of figure 18). This is maximum ($C \simeq 0.013$) for $N = 0$ at small t^*, but decreases over

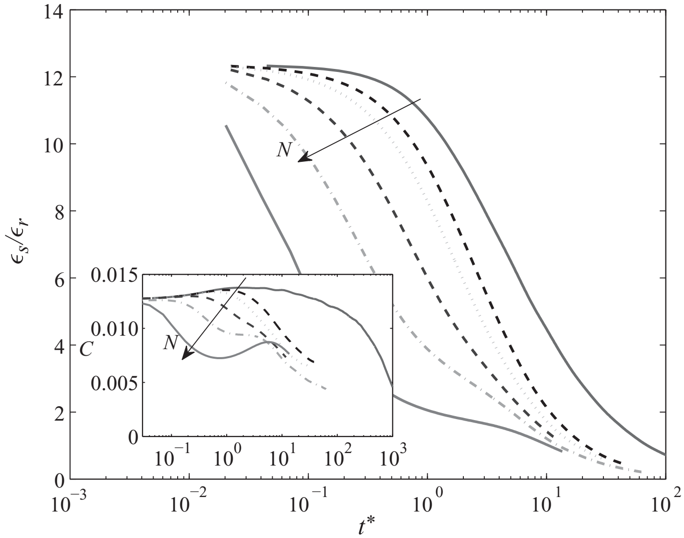

FIGURE 18. Ratio of the subgrid-scale term to the resolved term of the viscous dissipation rate. Inset: profile of the Smagorinsky constant as computed from the dynamic model.

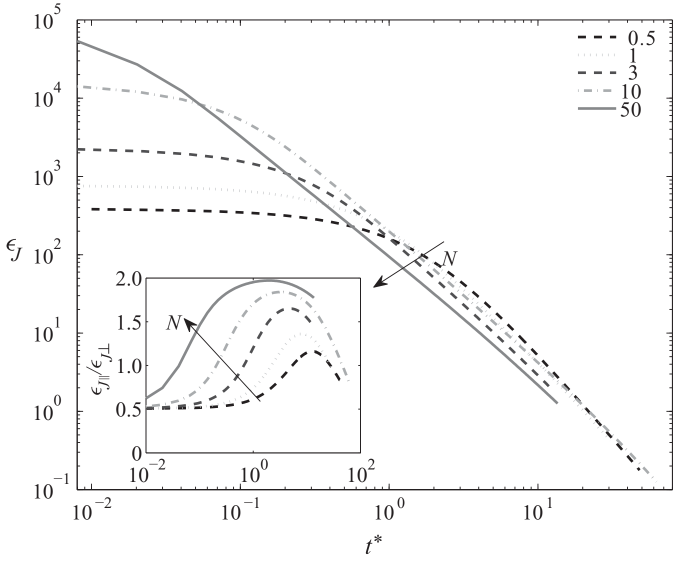

FIGURE 19. Joule dissipation rate. Inset: ratio of the contributions from parallel and perpendicular velocity components.

time and with N, reflecting a lesser contribution from the subgrid scales. A similar behaviour was observed in other self-adapting LES of MHD turbulence (Knaepen & Moin 2004; Vorobev & Zikanov 2008) and LES of turbulence in the presence of strong stratification or rotation (Mathieu & Scott 2000).

The time evolution of Joule dissipation is reported in figure 19. At $t = 0$, when the velocity field is isotropic at small and large scales, ϵ_J is directly proportional to the interaction parameter. Subsequently, the decay of ϵ_J depends on two factors: the decrease of kinetic energy and the rise of the velocity gradients anisotropy; see (2.6).

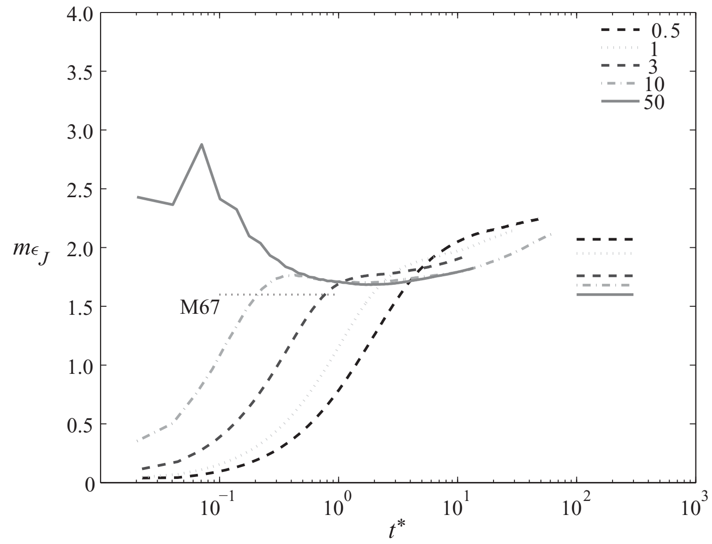

FIGURE 20. Decay exponent of the Joule dissipation rate.

Furthermore, since the bulk of the kinetic energy is at large scales, their anisotropy will have more impact on ϵ_J, as opposed to the small-scale anisotropy. In figure 19, one can see that the developing anisotropy of gradients leads to weaker Joule dissipation in flows with stronger magnetic field.

Before discussing the decay law of the Joule dissipation, we consider the ratio of the contributions to ϵ_J from the different velocity components (inset of figure 19). All distributions of $\epsilon_{J\parallel}/\epsilon_{J\perp}$ start at 1/2. Then, the ratios increase during the decay, with case $N = 50$ attaining the limit of 2. These two values correspond to the isotropic state and the prediction of the linear theory, respectively. Given the solution (2.24) and the expression for ϵ_J in Fourier space (2.6), the ratio can be written as

$$\frac{\epsilon_{J\parallel}(t/\tau)}{\epsilon_{J\perp}(t/\tau)} \doteq \frac{\displaystyle\int_0^{\pi} \sin^2(\psi)\cos^2(\psi)\exp\left[-2\cos^2(\psi)\frac{t}{\tau}\right]\mathrm{d}\psi}{\displaystyle\int_0^{\pi} \tfrac{1}{2}\left[1+\cos^2(\psi)\right]\sin(\psi)\cos^2(\psi)\exp\left[-2\cos^2(\psi)\frac{t}{\tau}\right]\mathrm{d}\psi}. \tag{4.7}$$

At $t/\tau = 0$ in isotropic turbulence, the ratio becomes

$$\left.\frac{\epsilon_{J\parallel}}{\epsilon_{J\perp}}\right|_{t=0} = \frac{1}{2}, \tag{4.8}$$

while for $t/\tau = \infty$

$$\left.\frac{\epsilon_{J\parallel}}{\epsilon_{J\perp}}\right|_{t=\infty} = 2. \tag{4.9}$$

Like (2.30), (4.8) and (4.9) are independent of the initial conditions of the velocity field. As observed for the kinetic energy component, deviations from (4.9) are inherent to the nonlinear evolution of the flow.

The decay exponents of $\epsilon_J, \epsilon_{J\perp}$ and $\epsilon_{J\parallel}$ are plotted in figures 20–22. Similarly to the other two terms of the kinetic energy budget, ϵ_J and more especially $\epsilon_{J\perp}$ display a power law. Accordingly, at later times the exponent $m_{J\perp}$ closely matches $m_{\nu\perp}$ and $(m_\perp + 1)$. This observation allows some general conclusions regarding the kinetic

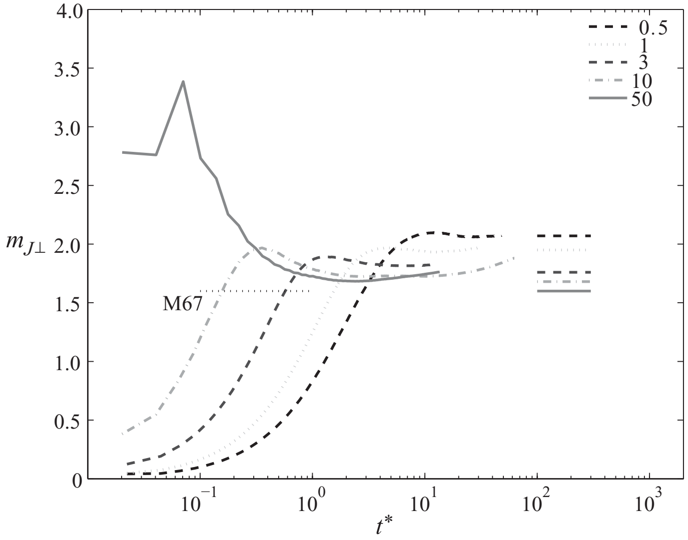

FIGURE 21. Decay exponent of the perpendicular component of the Joule dissipation rate. Horizontal lines on the right side are at $m_\perp + 1$, with $m_\perp$ estimated from the second plateau of figure 5.

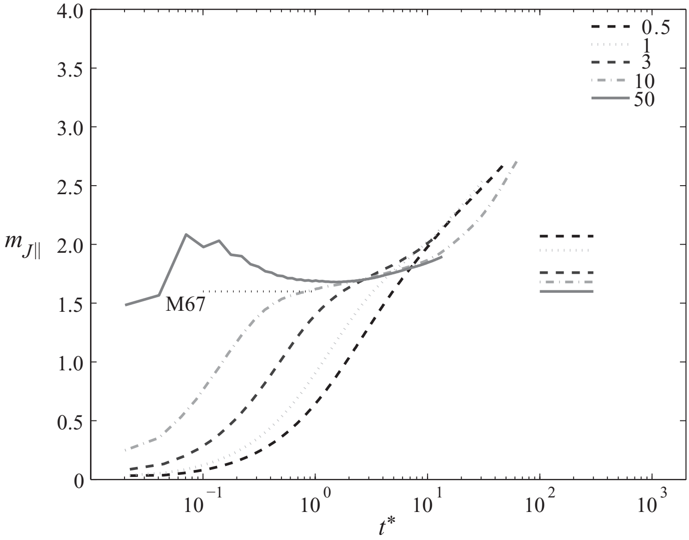

FIGURE 22. Decay exponent of the parallel component of the Joule dissipation rate. Horizontal lines on the right side are at $m_\perp + 1$, with $m_\perp$ estimated from the second plateau of figure 5.

energy budget. At intermediate values of N and large times, all three terms should be taken into account in the kinetic energy budget of the perpendicular component, i.e.

$$\frac{\mathrm{d}}{\mathrm{d}t}K_\perp = -\epsilon_{\nu\perp} - \epsilon_{J\perp}. \tag{4.10}$$

The power law

$$K_\perp \sim t^{-m_\perp} \tag{4.11}$$

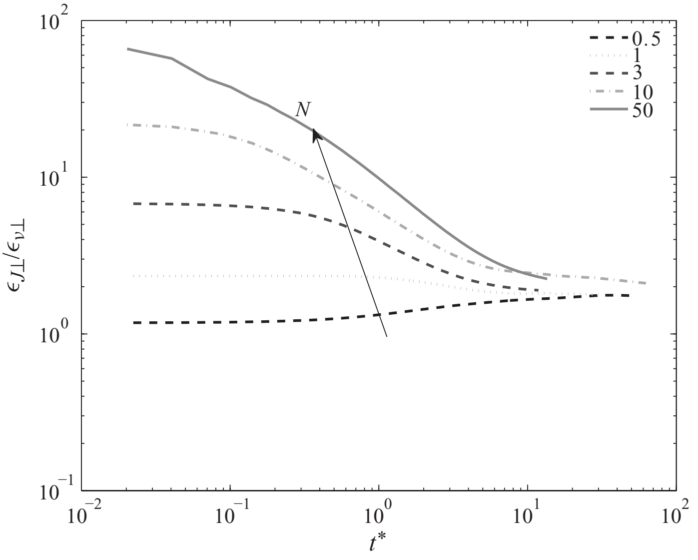

FIGURE 23. Ratio of Joule to viscous dissipation: perpendicular component.

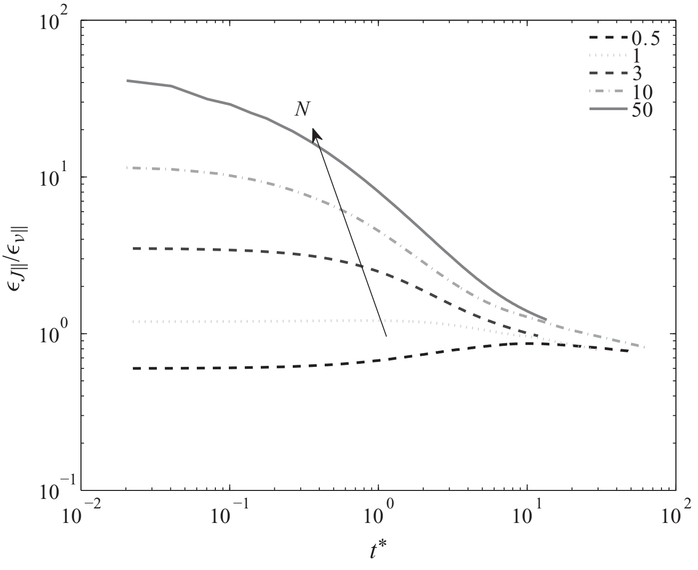

FIGURE 24. Ratio of Joule to total viscous dissipation: parallel component.

is possible only if

$$\epsilon_{J\perp} \sim t^{-m_\perp - 1}, \tag{4.12}$$

$$\epsilon_{\nu\perp} \sim t^{-m_\perp - 1}. \tag{4.13}$$

The last two relations imply that the ratio $\epsilon_{J\perp}/\epsilon_{\nu\perp}$ is constant. This can be verified directly from the numerical data, as illustrated in figure 23. For $t^* > 10$, the ratios converge towards a constant value, which, remarkably, is of order 1 for all the cases. Furthermore, figures 24 and 25 show that such equilibrium is also achieved by the parallel component, and therefore by the sum of the two components. It can be

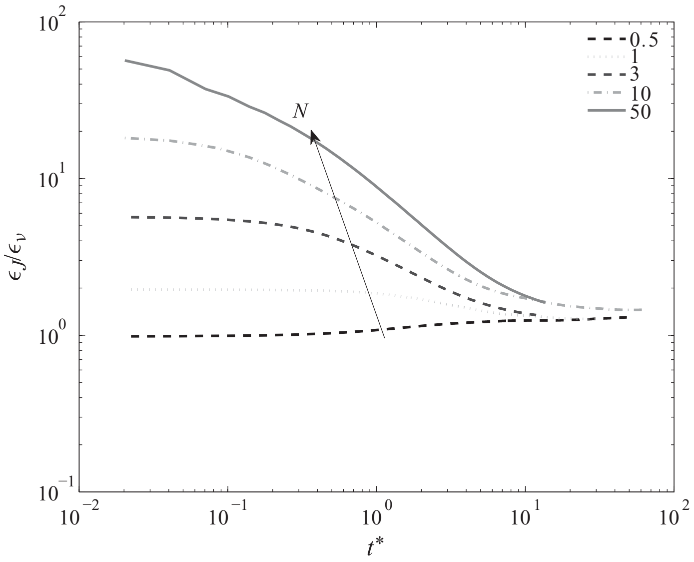

FIGURE 25. Ratio of Joule to total viscous dissipation.

argued that since $\epsilon_{\nu\parallel}$ does not clearly display a power law, its establishment is only a sufficient but not a necessary condition for the equilibrium. By recognizing that the ratio ϵ_J/ϵ_ν has the form of the square of the Hartmann number Ha, one concludes that within the time interval considered but irrespective of the value of N, the flow evolves towards a condition of Ha of order unity. This represents an equipartition of the dissipations.

4.2.1. *Anisotropy invariants*

We conclude the analysis of the dissipation terms by considering their invariants. Similarly to the anisotropy at the large scales, the type and degree of anisotropy at small scales can be described by the anisotropy tensor of the viscous dissipation

$$d_{\nu_{ij}} = \frac{\epsilon_{\nu_{ij}}}{2\epsilon_\nu} - \frac{1}{3}\delta_{ij}, \tag{4.14}$$

which is traceless and has two non-trivial invariants $6\eta_\nu^2 = d_{\nu_{ij}}d_{\nu_{ji}}$ and $6\xi_\nu^3 = d_{\nu_{ij}}d_{\nu_{jk}}d_{\nu_{ki}}$. Figure 26 indicates that the small-scale fluctuations depart from isotropy, as the magnetic field intensifies. This lack of 'local isotropy' is evidently one of the reasons why the phenomenological arguments of Kolmogorov are inapplicable to MHD turbulence. Comparing the curves of $d_{\nu_{ij}}$ with those of b_{ij} in figure 12, one sees that the peak of anisotropy occurs earlier in time for the large scales compared to the small scales. By the time when b_{ij} is temporarily back to the isotropic condition, the small scales are strongly anisotropic. This lag between the two phases suggests that the transfer of energy between different velocity components takes place at different time scales depending on the length scale. For completeness, the AIM of $d_{\nu_{ij}}$ is reported in figure 27.

The anisotropy tensor of the Joule dissipation

$$d_{J_{ij}} = \frac{\epsilon_{J_{ij}}}{2\epsilon_J} - \frac{1}{3}\delta_{ij} \tag{4.15}$$

is shown in figure 28. Unlike b_{ij}, $d_{J\parallel}$ can intersect the axis of isotropy twice, or never if N is small. The asymptotes for $t \to 0$ and $t \to \infty$, obtained from (4.8) and (4.9), are

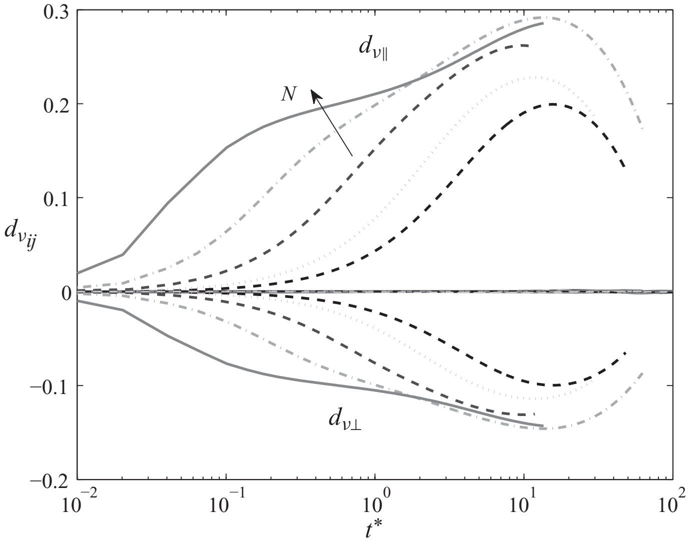

FIGURE 26. Components of the viscous dissipation anisotropy tensor.

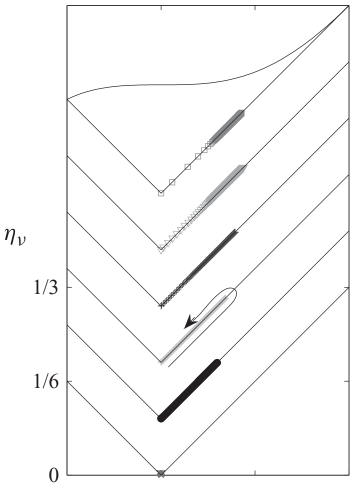

FIGURE 27. AIM of viscous dissipation tensor. $N = 0$ (values are on the origin), $N = 0.5$, 1, 3, 10, 50 (shifted progressively upwards by 0.1). The arrow indicates the direction of the path.

$d_{J\parallel 0} = 1/15$ and $d_{J\parallel\infty} = 1/6$. As illustrated in figure 28, the second limit is reached only at $N = 50$.

The AIM of $d_{J_{ij}}$ (figure 29) is constrained to the straight sides of Lumley triangle with the two limiting positions (corresponding to the asymptotes):

$$\eta_{J0} = \left(d^2_{J_{ii}}/6\right)^{1/2} = 1/15, \tag{4.16}$$

$$\xi_{J0} = \left(d^3_{J_{ii}}/6\right)^{1/3} = -1/15, \tag{4.17}$$

and

$$\eta_{J\infty} = \xi_{J\infty} = (2^2 \times 3)^{-1}, \tag{4.18}$$

which are identical to $(\eta_\infty, \xi_\infty)$.

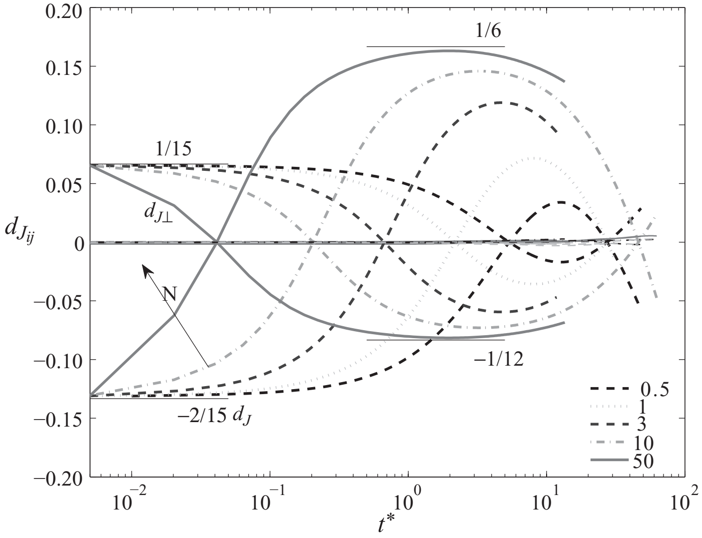

FIGURE 28. Anisotropy invariants of the Joule dissipation tensor.

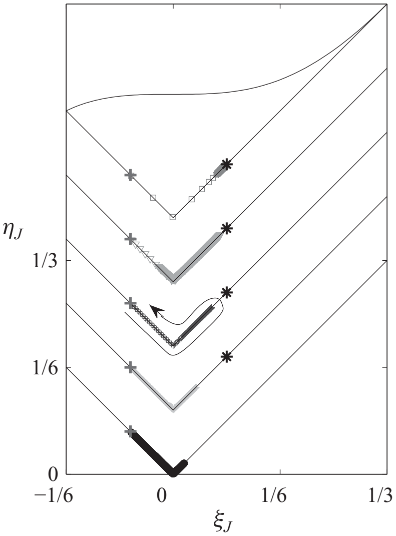

FIGURE 29. AIM of the Joule dissipation tensor. N = 0.5, 1, 3, 10, 50, 50 (each shifted progressively upwards by 0.1). The plus denotes the starting point (η_{J0}, ξ_{J0}), while the asterisk marks the limit state for $(\eta_{J\infty}, \xi_{J\infty})$. The arrow indicates the direction of the path.

A different view on the small-scale anisotropy is provided by the ratios of the derivatives (e.g. Vorobev *et al.* 2005; Vorobev & Zikanov 2008)

$$G_{ii} = \frac{1}{2}\frac{\overline{(\partial_3 u_i)^2}}{\overline{(\partial_i u_i)^2}}, \quad i = 1, 2, \tag{4.19}$$

$$G_{3i} = 2\frac{\overline{(\partial_3 u_3)^2}}{\overline{(\partial_i u_3)^2}}, \quad i = 1, 2, \tag{4.20}$$

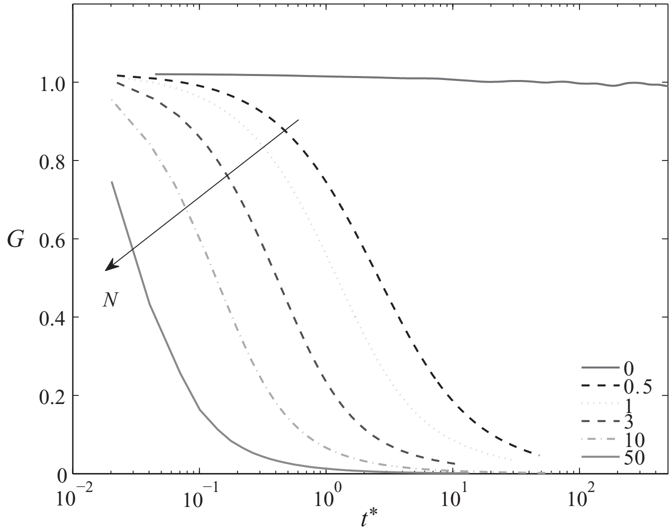

FIGURE 30. Coefficients of the gradients anisotropy; see (4.21).

which are unitary in isotropic turbulence (e.g. George & Hussein 1991). The single terms of (4.19) and (4.20) correspond to the derivative at the origin of the longitudinal and transverse structure functions of order 2. As in Vorobev *et al.* (2005), we consider the average

$$G = \frac{G_{22} + G_{32}}{2}, \tag{4.21}$$

which are presented in figure 30. In agreement with the approach towards a two-dimensional turbulent state observed before, all distributions tend to zero. In previous work at moderate values of N (Zikanov & Thess 1998), where turbulence was forced, the temporal profiles of G displayed a quasi-periodic behaviour, with bursts at high intensity followed by quiescent intervals. No such intermittency is observed in the present simulations of decaying turbulence.

4.2.2. *Derivative skewness*

In hydrodynamic turbulence, the skewness of the velocity derivative quantifies the importance of the nonlinear term with respect to viscous dissipation. This is evident from its definition in spectral space:

$$S = -\frac{3 \times 30^{1/2}}{14} \frac{\displaystyle\int_0^\infty k^2 T(k)\,\mathrm{d}k}{\left[\displaystyle\int_0^\infty k^2 E(k)\,\mathrm{d}k\right]^{3/2}}, \tag{4.22}$$

which involves the nonlinear transfer. Figures 31 and 32 report the skewness of the three velocity components computed according to (3.2). Whereas $S_\perp$ and $S_\parallel$ are $\simeq -0.5$ throughout the decay for $N = 0$ (as is typical of HIT at the current values of R_λ; Burattini, Lavoie & Antonia 2008*c*), for $N > 0$ both coefficients tend to zero at sufficiently large times, with increasing N. However, there are differences as well: while $S_\perp$ always increases monotonically, the behaviour of $S_\parallel$ depends markedly on the value of N. When this is small, $S_\perp$ has a local minimum, which disappears at

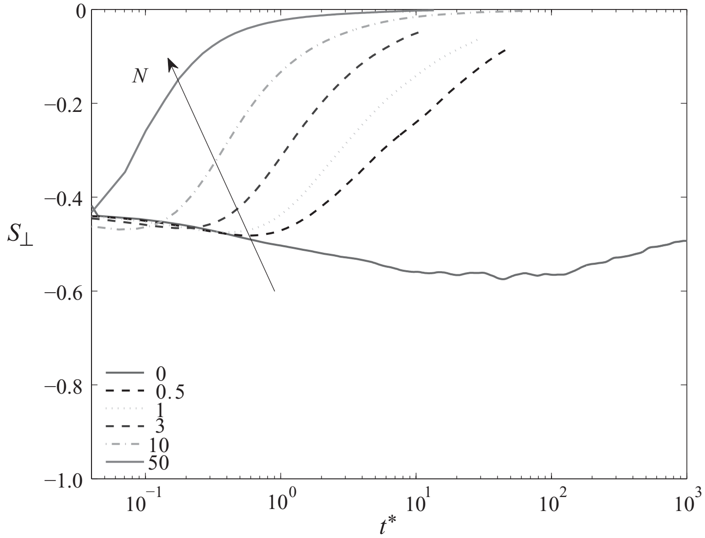

Figure 31. Derivative skewness of the perpendicular velocity component.

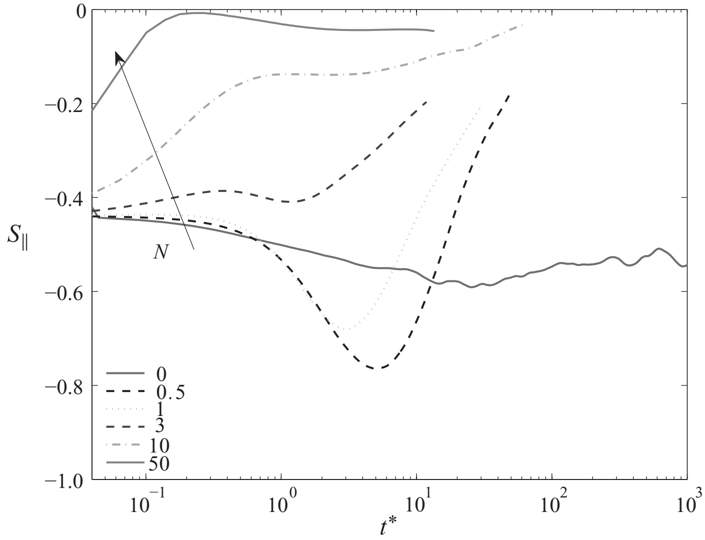

Figure 32. Derivative skewness of the parallel velocity component.

large N. The fact that at low N, the nonlinear effects are stronger for $u_\parallel$ than $u_\perp$ is consistent with the larger variation experienced by the parallel component of the kinetic energy. For example, at $N = 1$, $m_\parallel$ (figure 6) takes a wider range of values, compared to $m_\perp$ (figure 5), and therefore $u_\parallel$ seemingly experiences a larger nonlinear transfer among the length scales. Schumann (1976) showed that the skewness defined as in (4.22) was substantially unaffected by N, when this was $\leqslant 50$. However, his time of application of $\boldsymbol{B}_0$ was rather short ($0.4 < t^* < 1.2$). Crucially, the present simulations show that both $S_\perp$ and $S_\parallel$ tend to zero at sufficiently large times. The absence of this trend was interpreted by Schumann (1976) as the persistence of three-dimensional features of the flow. Note that in the forced MHD turbulence, which is

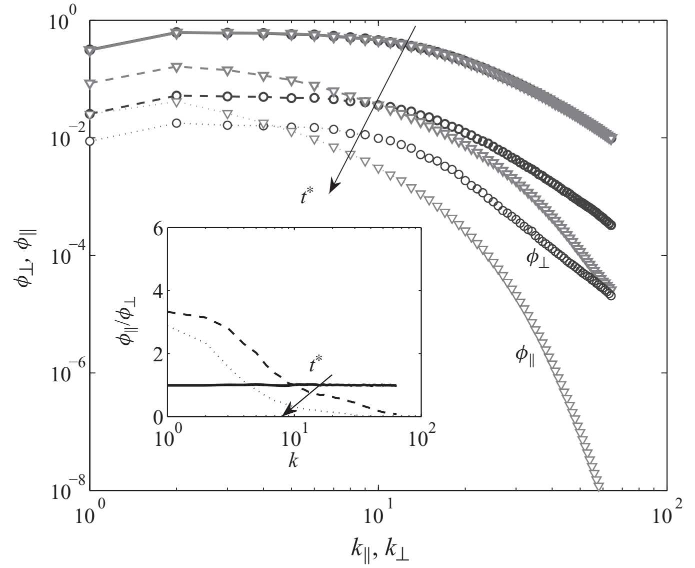

FIGURE 33. One-dimensional spectra of the velocity components for $N = 0.5$. ∇, $\phi_\parallel$; $\circ$, $\phi_\perp$. $t^* = 0$ (solid line), $t^* = 8.8$ (dashed line), $t^* = 32$ (dotted line). The values of the kinetic energy components are: $K_\parallel = 1.1$ and $K_\perp = 0.78$, for $t^* = 8.8$; $K_\parallel = 0.17$ and $K_\perp = 0.20$, for $t^* = 32$.

statistically stationary, the difference between $S_\perp$ and $S_\parallel$ might be smaller. For $N = 1$, Ishida & Kaneda (2007) reported a value of $\simeq -0.2$ for both components, while Kinet *et al.* (2008) obtained $S_\parallel = -0.41$ and $S_\perp = -0.54$.

4.3. *Spectra*

Further insight into the evolution of the kinetic energy components is provided by the one-dimensional spectra defined by (2.8). Their typical behaviour is illustrated in figure 33 for $N = 0.5$ (at larger N, results are qualitatively similar). Over time, as the flow is affected by Joule dissipation, both $\phi_\perp$ and $\phi_\parallel$ are attenuated at large k. This phenomenon has been observed in earlier simulations, e.g. Schumann (1976) and Zikanov & Thess (1998). However, the present results further show that the reduction is faster for $\phi_\parallel$ than for $\phi_\perp$ (i.e. $\phi_\parallel/\phi_\perp < 1$ at large k; see the inset of figure 33). Note that this is nonetheless consistent with the relation $\epsilon_{\nu\parallel} > \epsilon_{\nu\perp}$ (figure 16) because for the three-dimensional spectra – which directly yield the dissipation components via (2.10) – it holds that $E_\parallel/E_\perp > 1$ at large k. As noted in Burattini *et al.* (2008*a*), this difference between one-dimensional and three-dimensional distributions follows directly from the type of anisotropy induced by the magnetic field.

The one-dimensional spectra of MHD turbulence are often inspected to verify the presence of the k^{-3} power law. Alemany *et al.* (1979) derived such law assuming that at each wavenumber, there exists a quasi-equilibrium between Joule dissipation and angular energy transfer in spectral space, for both $\phi_\parallel(k)$ and $\phi_\perp(k)$. While earlier experimental results (Kolesnikov & Tsinober 1972; Alemany *et al.* 1979) performed at low N seemed to support this prediction (although the two components were never measured simultaneously), more recent simulations (Ishida & Kaneda 2007; Burattini *et al.* 2008*b*) and experiments (Eckert *et al.* 2001) have questioned such behaviour. Figures 34 and 35 show that for $N = 0.5$ and 10, the compensated spectra have varying slopes but neither displays a robust plateau. The lack of support for the k^{-3}

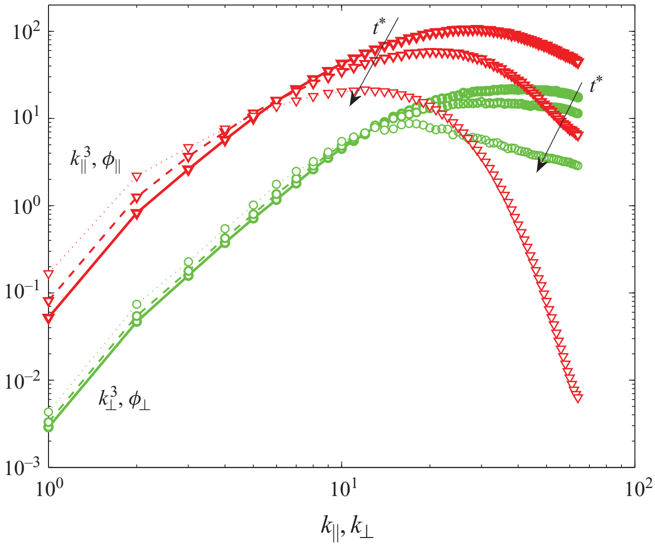

FIGURE 34. (Colour online) One-dimensional spectra compensated by k^3, $N = 0.5$. ∇, $\phi_{\parallel}$; $\bigcirc$, $\phi_{\perp}$. (These values are shifted downwards by one decade, for clarity.) $t^* = 3.1$ (solid line), $t^* = 8.8$ (dashed line) and $t^* = 32$ (dotted line).

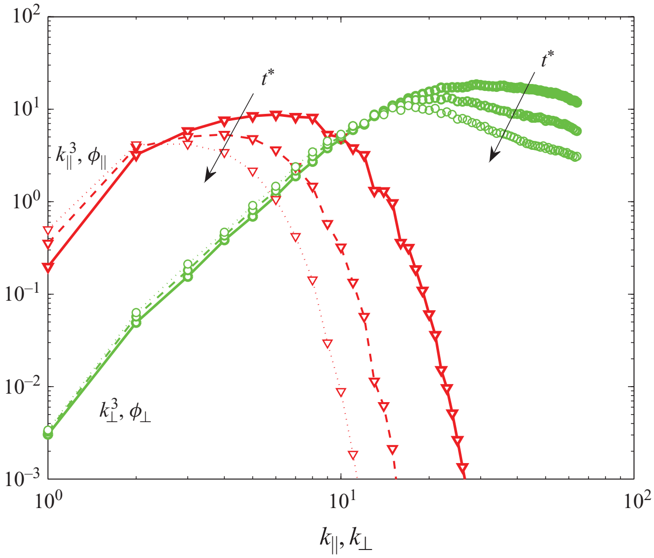

FIGURE 35. (Colour online) One-dimensional spectra compensated by k^3, $N = 10$. ∇, $\phi_{\parallel}$; $\bigcirc$, $\phi_{\perp}$. (These values are shifted downwards by one decade, for clarity.) $t^* = 6.0$ (solid line), $t^* = 19.2$ (dashed line) and $t^* = 41.2$ (dotted line).

law is perhaps not surprising. The arguments of Alemany *et al.* (1979) neglect viscous dissipation, while in reality, as illustrated in figure 23, the viscous and magnetic dissipation rates tend to be of the same order of magnitude at later stages of the decay.

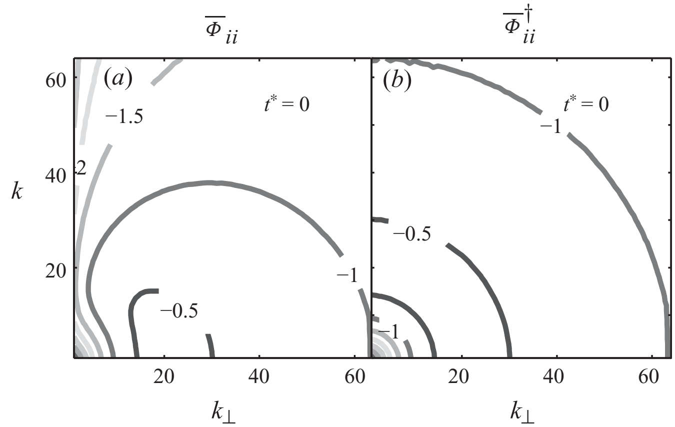

FIGURE 36. Contours of (*a*) $\log \overline{\Phi}_{ii}$ and (*b*) $\log \overline{\Phi}^{\dagger}_{ii}$ at the isotropic initial conditions.

For axisymmetric turbulence, the one-dimensional spectra provide only a partial description of the kinetic energy spectral distribution. Two-dimensional spectra, which do not suffer from the same limitation, are considered next. The two-dimensional form of $\Phi_{ii}(\boldsymbol{k})$ is given by

$$\overline{\Phi}_{ii}(k, \psi, t) = \frac{1}{2\pi} \int_0^{2\pi} \Phi_{ii}(k, \varphi, \psi, t)\, \mathrm{d}\varphi, \tag{4.23}$$

where the averaging (denoted by the overbar) is carried out over the homogeneous direction φ (figure 36*a*). In the following, the geometrical dependence on ψ of the spectra is eliminated by the transformation $\overline{\Phi}^{\dagger}_{ii} = \overline{\Phi}_{ii}/\sin(\psi)$. In the isotropic case, the contours of $\overline{\Phi}^{\dagger}_{ii}$ thus become arcs of a circle; see figure 36(*b*).

Figure 37 presents the two-dimensional spectra computed at different times for $N = 0.5$. One can see that the initial distribution of $\overline{\Phi}^{\dagger}_{\perp}$ is rapidly eroded near the $k_\parallel$ axis (where most of its energetic content is initially localized) by the applied magnetic field. Conversely, at small times $\overline{\Phi}^{\dagger}_{\parallel}$ is relatively unaffected. As time increases, the two sets of contours converge to a similar shape. At $t^* = 81$, the characteristics of both $\overline{\Phi}^{\dagger}_{\perp}$ and $\overline{\Phi}^{\dagger}_{\parallel}$ resemble the eigenfunctions of the total (viscous and Joule) dissipation in the linear problem given by

$$f(\boldsymbol{k}) = c\nu k^2 + \frac{\sigma B_0^2}{\rho} \frac{k_3^2}{k^2}. \tag{4.24}$$

These are plotted in figure 38 as a function of $k_\perp = k \sin(\psi)$ and $k_\parallel = k \cos(\psi)$ and divided by $\sin(\psi)$. The properties of (4.24) have been studied by Pothérat & Alboussière (2003), who showed that the least dissipative modes of the flow are located within the curves $f(\boldsymbol{k})$=const. Dymkou & Pothérat (2008) suggested that the iso-contours of the two-dimensional energy spectra of the full nonlinear problem tend to follow the same curves, which is confirmed by the present results.

Figure 37 prompts a comment on a commonly accepted picture of decaying MHD turbulence. After Moffatt (1967), it is often stated (e.g. Davidson 1997) that following the application of $\boldsymbol{B}_0$, the kinetic energy is ‘channelled’ into the parallel component. This statement can be misleading as it suggests that the $K_\perp$ component loses energy to the benefit of $K_\parallel$. In reality, as shown by the present simulations, the latter component remains relatively unaffected by the sudden application of $\boldsymbol{B}_0$, whereas $K_\perp$ is strongly

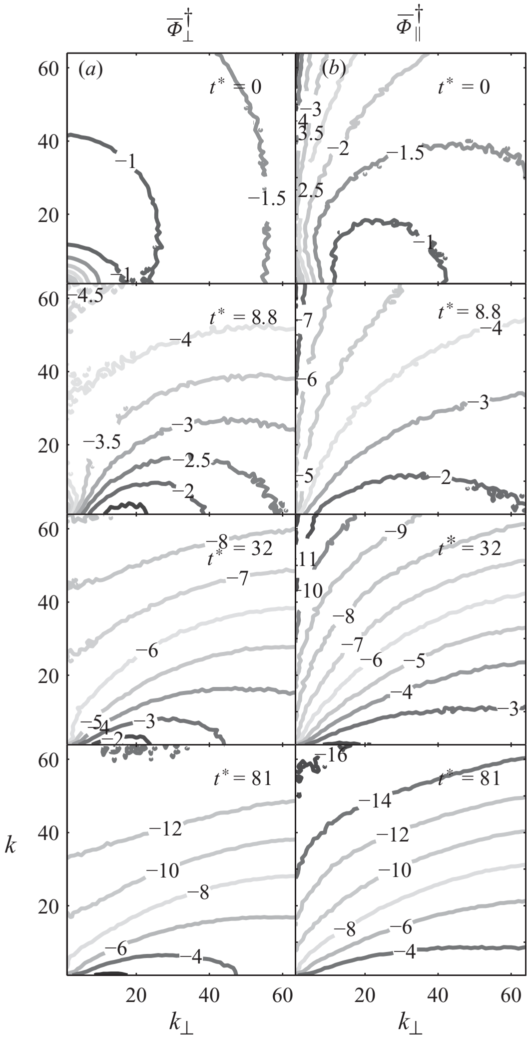

FIGURE 37. Contours of (*a*) $\log \overline{\Phi}^{\dagger}_{\perp}$ and (*b*) $\log \overline{\Phi}^{\dagger}_{\parallel}$ at different times during the decay; $N = 0.5$. Time increases from top to bottom ($0 < t^* < 81$).

suppressed during the initial stage. The apparent growth of $K_{\parallel}$ is relative only to the behaviour of $K_{\perp}$.

The two-dimensional distributions of the Joule dissipation are strictly related to those of $\overline{\Phi}^{\dagger}_{\perp}$ and $\overline{\Phi}^{\dagger}_{\parallel}$. Their evolution, reported in figure 39, highlights the large-scale nature of ϵ_J and the increasing similarity between the two velocity components. It is also evident that the maximum of ϵ_J shifts towards larger values of ψ, as the energy near $k_{\parallel}$ is being dissipated. This gradual shift suggests that the concept of a stationary dissipation cone is inapplicable in the case of decaying turbulence.

5. Conclusions

The first conclusion of this study is that the decay follows a complex path that cannot be fully described by any of the existing theoretical models. In particular,

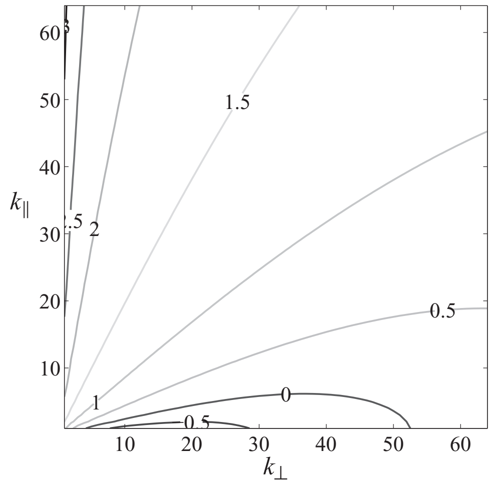

FIGURE 38. Eigenfunctions of the total dissipation of the kinetic energy.

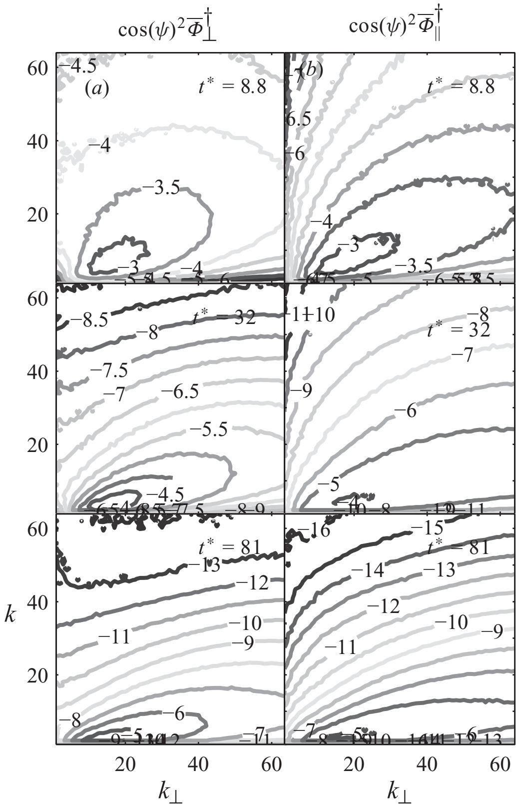

FIGURE 39. Contours of the components of Joule dissipation represented as (*a*) $\log[\cos^2(\psi)\,\overline{\Phi}^\dagger_\perp]$ and (*b*) $\log[\cos^2(\psi)\,\overline{\Phi}^\dagger_\parallel]$ at different times during the decay; $N = 0.5$. Time increases from top to bottom ($8.8 < t^* < 81$).

our simulations show that the linearized behaviour, which was earlier considered by Moffatt (1967) and computed by Schumann (1976), is followed only for a short time. We find that the nonlinear effects rapidly dominate (after one eddy turnover time) the flow evolution. As a consequence, the repartition of the kinetic energy between the velocity components quickly becomes the opposite of that suggested by the linear theory.

Regarding the establishment of the initial power law for the decay of the kinetic energy, our results confirm the validity of the $t^{-1/2}$ decay. The data also show that later, in the nonlinear regime, the velocity components in the direction parallel and perpendicular to the magnetic field decay at different rates. This reconciles the apparent discrepancies between earlier experiments in grid turbulence.

As an entirely new and rather unexpected result, we observe that at the late stages of the decay, approximately after $10t^*$, the flow evolves into a state in which the viscous and Joule dissipation rates are nearly equal and only weakly sensitive to the strength of the magnetic field. The existence of such a 'nearly universal' state with equipartition between the viscous and Joule dissipation rates may serve as a basis for the development of theories of MHD turbulence decay.

From the computational point of view, we conclude that dynamic LES can be a useful tool for simulating MHD turbulence at low Re_m and large N. In fact, since Joule dissipation introduces a sink of the energy proportional to the amplitude of the velocity fluctuation at each wavenumber, overall the large scales are a significant contributor to the kinetic energy dissipation. Consequently, as the role of the energy cascade is less dominant compared to hydrodynamic turbulence, small-scale modelling can save substantial computational resources.

Although the present flow remains overall axisymmetric and shearless throughout the decay, the anisotropy of the small and large scales is rather different. In inhomogeneous flows, such as the plane channel without magnetic field, the off-diagonal components of the Reynolds stress tensor are non-zero. However, the small scales are nearly isotropic away from the wall. It would thus be interesting to compare the present results with those in the MHD channel flow.

This work, conducted as part of the award (Modelling and simulation of turbulent conductive flows in the limit of low magnetic Reynolds number) made under the European Heads of Research Councils and the European Science Foundation EURYI (European Young Investigator) Awards scheme, was supported by funds from the Participating Organizations of EURYI and the EC Sixth Framework Programme. Financial support from the Communauté Française de Belgique (ARC 02/07-283) and from the contract of association EURATOM-Belgian state is also gratefully acknowledged. The content of the publication is the sole responsibility of the authors and it does not necessarily represent the views of the Commission or its services.

REFERENCES

Alemany, A., Moreau, R., Sulem, P. L. & Frisch, U. 1979 Influence of an external magnetic field on homogeneous MHD turbulence. *J. de Méc.* **18**, 277–313.

Batchelor, G. K. 1967 *An Introduction to Fluid Dynamics*. Cambridge University Press.

Burattini, P., Kinet, M., Carati, D. & Knaepen, B. 2008*a* Anisotropy of velocity spectra in quasistatic magnetohydrodynamic turbulence. *Phys. Fluids* **20** (6), 065110-1–065110-5.

Burattini, P., Kinet, M., Carati, D. & Knaepen, B. 2008*b* Spectral energetics of quasi-static MHD turbulence. *Physica* D **237** (14–17), 2062–2066.

Burattini, P., Lavoie, P. & Antonia, R. A. 2005 On the normalized turbulent energy dissipation rate. *Phys. Fluids* **17**, 098103.

Burattini, P., Lavoie, P. & Antonia, R. A. 2008*c* Velocity derivative skewness in isotropic turbulence and its measurement with hot wires. *Exp. Fluids* **45** (3), 523–535.

Choi, K.-S. & Lumley, J. L. 2001 The return to isotropy of homogeneous turbulence. *J. Fluid Mech.* **436**, 59–84.

Comte-Bellot, G. & Corrsin, S. 1971 Simple Eulerian time correlation of full- and narrow-band velocity signals in grid-generated, 'isotropic' turbulence. *J. Fluid Mech.* **48**, 273–337.

Davidson, P. A. 1995 Magnetic damping of jets and vortices. *J. Fluid Mech.* **299**, 153–186.

Davidson, P. A. 1997 The role of angular momentum in the magnetic damping of turbulence. *J. Fluid Mech.* **336**, 123–150.

Davidson, P. A. 2001 *An Introduction to Magnetohydrodynamics*. Cambridge University Press.

Dymkou, V. & Pothérat, A. 2008 Spectral methods for low-Rm MHD turbulence. In *Proceedings of the 7th International PAMIR Conference. Fundamental and Applied MHD* (ed. J.-P. Chopart), vol. 2, pp. 393–397. Université de Reims Champagne-Ardenne.

Eckert, S., Gerbeth, G., Witke, W. & Langenbrunner, H. 2001 MHD turbulence measurements in a sodium channel flow exposed to a transverse magnetic field. *Intl J. Heat Fluid Flow* **22**, 358–364.

George, W. K. & Hussein, H. J. 1991 Locally axisymmetric turbulence. *J. Fluid Mech.* **233**, 1–23.

George, W. K., Wang, H., Wollblad, C. & Johansson, T. 2001 Homogeneous turbulence and its relation to realizable flows. In *14th Australasian Fluid Mechanics Conference* (ed. B. B. Dally), pp. 41–48. Adelaide University.

Germano, M., Piomelli, U., Moin, P. & Cabot, W. H. 1991 A dynamic subgrid-scale eddy viscosity model. *Phys. Fluids* A **3**, 1760–1765.

Ishida, T., Davidson, P. & Kaneda, Y. 2006 On the decay of isotropic turbulence. *J. Fluid Mech.* **564**, 455–475.

Ishida, T. & Kaneda, Y. 2007 Small-scale anisotropy in magnetohydrodynamic turbulence under a strong uniform magnetic field. *Phys. Fluids* **19**, 075104-1–075104-10.

Kinet, M., Burattini, P., Carati, D. & Knaepen, B. 2008 Decay of passive scalar fluctuations in homogeneous magnetohydrodynamic turbulence. *Phys. Fluids* **20**, 075105-1–075105-12.

Knaepen, B., Kassinos, S. & Carati, D. 2004 Magnetohydrodynamic turbulence at moderate magnetic Reynolds number. *J. Fluid Mech.* **513**, 199–220.

Knaepen, B. & Moin, P. 2004 Large-eddy simulation of conductive flows at low magnetic Reynolds number. *Phys. Fluids* **16**, 1255–1261.

Kolesnikov, Y. & Tsinober, A. 1972 An experimental study of two-dimensional turbulence behind a grid. *Fluid Dyn.* **9**, 621–624.

Lehnert, B. 1955 The decay of magneto-turbulence in the presence of a magnetic field and Coriolis force. *Q. Appl. Math.* **12**, 321–341.

Lilly, D. K. 1992 A proposed modification of the Germano subgrid-scale closure method. *Phys. Fluids* **4** (3), 633–635.

Mathieu, J. & Scott, J. 2000 *An Introduction to Turbulent Flow*. Cambridge University Press.

Matthaeus, W. H., Ghosh, S., Oughton, S. & Roberts, D. A. 1996 Anisotropic three-dimensional MHD turbulence. *J. Geophys. Res.* **101**, 7619–7630.

Mininni, P. 2007 Inverse cascades and α effect at a low magnetic Prandtl number. *Phys. Rev.* E **76** (2), 026316.

Moffatt, H. K. 1967 On the suppression of turbulence by a uniform magnetic field. *J. Fluid Mech.* **28**, 571–592.

Moreau, R. 1990 *Magnetohydrodynamics*. Kluwer Academic.

Moreau, R., Thess, A. & Tsinober, A. 2007 MHD turbulence at low magnetic Reynolds number: present understanding and future needs. In *Magnetohydrodynamics – Historical Evolution and Trends* (ed. S. Molokov, R. Moreau & H. K. Moffatt), vol. 80, pp. 231–246. Springer.

Müller, U. & Bühler, L. 2001 *Magnetofluiddynamics in Channels and Containers*. Springer.

Oughton, S., Priest, E. R. & Matthaeus, W. H. 1994 The influence of a mean magnetic field on three-dimensional MHD turbulence. *J. Fluid Mech.* **280**, 95–117.

Ponty, Y., Mininni, P., Montgomery, D., Pinton, J.-F., Politano, H. & Pouquet, A. 2005 Numerical study of dynamo action at low magnetic Prandtl numbers. *Phys. Rev. Lett.* **94** (16), 164502.

Pope, S. B. 2000 *Turbulent Flows*. Cambridge University Press.

Pothérat, A. & Alboussière, T. 2003 Small scales and anisotropy in low Rm magnetohydrodynamic turbulence. *Phys. Fluids* **15**, 3170–3180.

Roberts, P. H. 1967 *An Introduction to Magnetohydrodynamics*. Elsevier.

Schumann, U. 1976 Numerical simulation of the transition from three- to two-dimensional turbulence under a uniform magnetic field. *J. Fluid Mech.* **74**, 31–58.

Shebalin, J., Matthaeus, W. H. & Montgomery, D. 1983 Anisotropy in MHD turbulence due to a mean magnetic field. *J. Plasma Phys.* **29**, 525–547.

Sommeria, J. & Moreau, R. 1982 Why, how, and when, MHD turbulence becomes two-dimensional. *J. Fluid Mech.* **118**, 507–518.

Vorobev, A. & Zikanov, O. 2008 Smagorinsky constant in LES modeling of anisotropic MHD turbulence. *Theor. Comp. Fluid Dyn.* **22**, 317–325.

Vorobev, A., Zikanov, O., Davidson, P. A. & Knaepen, B. 2005 Anisotropy of magnetohydrodynamic turbulence at low magnetic Reynolds number. *Phys. Fluids* **17**, 125105-1–125105-12.

Wang, H. & George, W. K. 2002 The integral scale in homogeneous isotropic turbulence. *J. Fluid Mech.* **459**, 429–443.

Williamson, J. H. 1980 Low-storage Runge–Kutta schemes. *J. Comput. Phys.* **35**, 48–56.

Yu, H., Girimaji, S. S. & Luo, L.-S. 2005 Lattice Boltzmann simulations of decaying homogeneous isotropic turbulence. *Phys. Rev.* E **71**, 016708.

Zikanov, O. & Thess, A. 1998 Direct numerical simulation of forced MHD turbulence at low magnetic Reynolds number. *J. Fluid Mech.* **358**, 299–333.